Engineering ligand reactivity enables high-temperature operation of stable perovskite solar cells

So Min Park,[1]† Mingyang Wei,[2]† Jian Xu,[1]† Harindi R. Atapattu,[3] Felix T. Eickemeyer,[2] Kasra Darabi,[4] Luke Grater,[1] Yi Yang,[6] Cheng Liu,[6] Sam Teale,[1] Bin Chen,[1,6] Hao Chen,[1] Tonghui Wang,[4] Lewei Zeng,[1] Aidan Maxwell,[1] Zaiwei Wang,[1] Keerthan R. Rao,[3] Zhuoyun Cai,[5] Shaik M. Zakeeruddin,[2] Jonathan T. Pham,[5] Chad M. Risko,[3] Aram Amassian,[4] Mercouri G. Kanatzidis,[6] Kenneth R. Graham,[3]* Michael Grätzel[2]* & Edward H. Sargent[1,6,7]*

[1]Department of Electrical and Computer Engineering, University of Toronto, 10 King's College Road, Toronto, Ontario, M5S 3G4, Canada

[2]Laboratory of Photonics and Interfaces, Ecole Polytechnique Fédérale de Lausanne, Lausanne, 1015, Switzerland

[3]Department of Chemistry, University of Kentucky, Lexington, KY, 40506, USA

[4]Department of Materials Science and Engineering, and Organic and Carbon Electronics Laboratories (ORaCEL), North Carolina State University, Raleigh, NC, 27695, USA

[5]Department of Chemical and Materials Engineering, University of Kentucky, Lexington, KY, 40506, USA

[6]Department of Chemistry, Northwestern University, Evanston, Illinois 60208, USA

[7]Department of Electrical and Computer Engineering, Northwestern University, Evanston, Illinois 60208, USA

† These authors contributed equally to this work.

* Corresponding authors. E-mails: ted.sargent@utoronto.ca; michael.graetzel@epfl.ch; kenneth.graham@uky.edu

Abstract: Perovskite solar cells (PSCs) consisting of interfacial two-dimensional/three-dimensional heterostructures that incorporate ammonium ligand intercalation have enabled rapid progress toward the goal of uniting performance with stability. However, as the field continues to seek ever-higher durability, additional tools that avoid progressive ligand intercalation are needed to minimize degradation at high temperatures. We use ammonium ligands that are nonreactive with the bulk of perovskites and investigate libraries varying ligand molecular structure systematically. We find that fluorinated aniliniums offer interfacial passivation and simultaneously minimize reactivity with perovskites. Using this approach, we report a certified quasi-steady-state PCE of 24.09% for inverted-structure PSCs. In an encapsulated device operating at 85 degrees Celsius and 50% relative humidity, we document a 1560-hour T_{85} at maximum power point under 1-sun illumination.

One-Sentence Summary: Suppressing ammonium ligand intercalation stabilizes the interface structure of perovskite solar cells at high temperatures.

Metal-halide perovskite solar cells (PSCs) are emerging photovoltaic (PV) technologies that hold promise in terawatt-scale deployment (*1*). They unite high power-conversion efficiencies (certified PCE up to 25.7%) (*2*) with low-cost solution processing using abundant materials (*3–5*). To compete with crystalline silicon (*c*-Si) solar cells and to be applied with *c*-Si in tandem cells, PSCs will need improved evidence of bankability (*6*), such as operating stability at elevated temperatures in accelerated aging (*7–12*).

Interfaces, which have high defect densities (*13*, *14*) and low barriers to ion transfer (*15*, *16*), and are susceptibility to moisture- and oxygen-induced degradation (*17*, *18*), can provide pathways for energy loss and degradation in PSCs (*19*, *20*). In record-efficiency PSCs, interfaces have been passivated by using two-dimensional/three-dimensional (2D/3D) hybrid structures (*21–23*), where a thin layer of Ruddlesden-Popper 2D perovskites terminates the 3D-pevovskite surface. These 2D/3D structures are constructed by exposing perovskite surfaces to a solution containing ammonium ligands, during which the 3D lattice is fragmented into 2D layers (*24*, *25*). This approach is beneficial because the 2D overlayer increases the resistance of perovskites to degradation (*17*, *26*).

There exists some diversity of findings in reports of the stability of 2D overlayers under stress. Some studies have indicated limited stability of the 3D/2D interface under thermal stress (*27–29*). Progress has been made, with a recent study demonstrating 500-hour operating stability under conditions of 65°C, 50% relative humidity, and maximum power point (MPP) tracking (ISOS-L-3-65°C), enhanced by the incorporation of 3-fluorophenethylammonium intercalation (*23*). Another report (*30*) that utilized an oleylammonium-intercalated 2D overlayer showed promising results in a 1000-hour damp-heat test, this study though reporting based on silicon PV module IEC 61215:2016 standards (85°C and 85% relative humidity, dark).

Given these promising performance stability improvements, the field continues to pursue ever-higher durability targets. There exists interest in raising the standard to 85°C ISOS-L-3 (MPP tracking at 85°C and 50% relative humidity). Here, the reactivity of ammonium ligands with 3D perovskites may lead to further penetration into the bulk perovskite film (*28*, *31*, *32*), and may contribute to deterioration in device performance under these very demanding stress conditions (*27*, *28*, *31–33*). Thus, we explored non-invasive surface-passivating ligands; but we did note that, in prior studies, these have yet to achieve the remarkable benefits of the 3D:2D strategy.

We sought to understand how molecular structure impacts ligand reactivity with 3D perovskites. Previous studies that used bulkier ammonium ligands to suppress the ligand intercalation, whereas certain small-sized ammonium ligands also exhibit low ligand reactivity (*34*, *35*). We attribute this difference to the limited availability of characterization techniques that allow one to compare ligand reactivity among different ammonium molecules – a particularly challenging pursuit in view of the ultrathin nature (typically < 10 nm) of the passivating overlayer (*23*).

Spectroscopy studies of ammonium ligands in perovskites

We used angle-resolved x-ray photoelectron spectroscopy (AR-XPS) and time-of-flight secondary ion mass spectrometry (TOF-SIMS) to investigate the penetration of a library of ammonium ligands into the bulk of perovskites (Fig. 1A), which include varying tail groups and alkyl chain lengths. A small-sized ammonium ligand, anilinium (An) had the lowest reactivity with 3D perovskites. We then explored derivatives of An with different degrees of fluorination to couple low ligand reactivity with effectual interfacial passivation. These molecules improved operating stability for the encapsulated PSC at 85°C and 50% relative humidity.

Ammonium ligands were deposited on $Cs_{0.05}MA_{0.05}FA_{0.9}Pb(I_{0.95}Br_{0.05})_3$ perovskite films (Methods), and films were annealed at 100°C (*31*). We used AR-XPS to probe the spatial distribution of ammonium ligands in the out-of-plane direction (Fig. 1B). AR-XPS is a non-destructive depth-profiling technique to determine the composition of ultrathin layers (< 10 nm) at the top surfaces of films (*36*, *37*). We varied the probe depth by changing the angle between the normal of the perovskite sample and the analyzer. Three different electron take-off angles (0°, 45°, and 75°) were selected with probe depths varying from approximately 6 to 8 nm at 0° to 1 to 2 nm at 75° (Fig. 1C).

To obtain the proportion of ammonium ligands at a given probe depth, we compared the ratio of C-N, where N signals originated from methylammonium (MA) and ammonium ligands at a binding energy of ~401.5 eV to the N signals originating from formamidinium (FA) at a binding energy of ~399.8 eV in the peak area in the N 1s XPS spectrum (figs. S1 and S2). The C-N/FA N ratio plots (Fig. 1D) revealed that the aryl ammoniums phenethylammonium (PEA) and 3-fluorophenethylammonium (3FPEA) had relatively uniform depth distributions, whereas alkyl ammoniums butylammonium (BA) and octylammonium (OA) tended to accumulate on the top surfaces, as evidenced by the C-N/FA N ratio increasing with larger electron take-off angles. However, each of the ligands yields C-N/FA N ratios were greater than those of untreated perovskites (control) for all electron take-off angles (Fig. 1E), indicating their distinct contributions to C-N signals and their intercalation into the bulk of perovskites.

We then examined long-chain alkyl ammonium decylammonium (DA), along with small-sized An (*34*, *35*, *38*). For DA, the C-N/FA N ratio decreased with a larger electron take-off angle (Fig. 1D). The reversed trend, as compared to other alkyl ammoniums, suggested that DA molecules diffused into the bulk of perovskites. In contrast, An exhibited low reactivity and had limited penetration into perovskites. The C-N/FA N ratios for An were ~2 times less than those for PEA at different electron take-off angles and are similar to control perovskites (Fig. 1E).

At these low C-N/FA N ratios, quantifying the extent of ligand penetration was difficult given the prominent C-N contribution from MA cations (fig. S2 and table S1). We thereby performed TOF-SIMS and found that, whereas PEA cations were distributed throughout the thickness of the perovskite film, An cations were detected only at the top surface of the film (fig. S3). The combining AR-XPS and TOF-SIMS support An remaining surface localized.

Although An exhibited low ligand reactivity, it has also been reported to have limited passivating capacity (*35*, *39*). To promote interfacial passivation, we explored fluorinated An, including 4-fluoroanilinium (4FAn), 2,6-difluoroanilinium (26FAn), and 3,4,5-trifluoroanilinium (345FAn), and tert-butyl-substituted 3,5-di-tert-butylanilinium (35tbuAn) (*17*, *40*, *41*). The C-N/FA N ratios (Fig. 1E) revealed that, compared to An, the newly-synthesized ligands retained similarly low reactivity with perovskites. For fluorinated An, this low reactivity was seen also in the C-F signal in the F 1s XPS spectrum (fig. S4). We identified a distinct C-F peak for 3FPEA, whereas the C-F signals from 4FAn, 26FAn, and 345FAn were all below the detection limit at the different electron take-off angles. TOF-SIMS confirmed that 345FAn cations were localized to the surface of the perovskite film (fig. S5).

We characterized the phase transformation of perovskites driven by their interaction with ammonium ligands. Ultrafast transient reflection (TR) spectroscopy was used initially to detect 2D perovskite formation (*42*). For the PEA-treated perovskite films, negative reflectance features associated with $n = 1$, 2, and 3 layered 2D perovskites were observed in the TR spectra (Fig. 2A). The relative proportion of 2D phases increased as the solution exposure time was prolonged (fig. S6) and was indicative of progressive phase transformation. For the An- and 345FAn-treated perovskite films, no 2D phases were observed (Fig. 2, B and C), which we attributed to their inability to convert 3D perovskites into 2D phases (fig. S7). These results reinforcing the model that inhibiting 2D phase conversion would also reduce ligand penetration.

Phase transformation was also investigated with grazing incidence wide-angle x-ray scattering (GIWAXS) measurements. Consistent with the TR studies, $n = 2$ 2D perovskites were observed at around $q = 0.29$ Å^{-1} along q_z for the PEA-treated perovskite film (Fig. 2D) that blocks vertical carrier transport (*32*). Incidence-angle-dependent diffraction patterns of PEA-treated perovskites revealed that the 2D phase formation was more pronounced near the surface (fig. S8). No 2D phase was detected in the An- and 345FAn-treated perovskites (Fig. 2, E and F).

We also observed formation of PbI_2 at $q = 0.9$ Å^{-1} for An-treated perovskite films, which we attributed to polar-solvent-induced decomposition during solution exposure, as seen in x-ray diffraction (XRD) characterization (fig. S9). GIWAXS characterization showed that 345FAn protected the underlying perovskites from this solvent-induced degradation (Fig. 2F). This is a topic that requires further in-depth investigation. We associate the reduction in surface degradation with increased hydrophobicity of this fluorinated ligand (fig. S10) (*26*).

Theoretical calculations

The interactions of ammonium ligands and perovskites are depicted in Fig. 3A. We performed density functional theory (DFT) calculations to explore how molecular structure impacted these interactions. We first calculated the binding energies (E_b) of two adjacent perovskite fragments at their interface with the insertion of ammonium ligands (Fig. 3B). A more negative E_b implies it is thermodynamically more favorable to form the 2D/3D heterostructures (*24*). Consistent with the

AR-XPS studies, penetrating PEA had a more negative E_b value than alkyl ammoniums OA and BA, whereas An and its derivatives showed the least tendency to form 2D/3D structures (Fig. 3C).

It has been suggested that the formation of 2D perovskites is related to the steric hindrance around the NH_3^+ group (*43*). We calculated the steric effect index (STEI, defined as the steric environment around the NH_3^+ group) of the ammonium ligand (*43*), and found that An had a much larger STEI of 2.34 than that of PEA (1.21). Furthermore, phase transformation entailed the replacement of A-site cations at 2D/3D interfaces (*24*). DFT calculations indicated that this process demanded more energy for An-intercalated interfaces compared to PEA-intercalated ones (fig. S11). This evidence further supported that An was less likely to penetrate the bulk of perovskites through ligand intercalation.

We proceeded to examine the interactions between ammonium ligands and perovskite surfaces. We calculated the interaction energy (E_{int}) for the scenario where an ammonium ligand occupied an MA-vacancy site on the perovskite surface (Fig. 3D). Electrostatic potential (ESP) calculations showed that fluorine substitution resulted in a higher positive charge density near the ammonium group (fig. S12) that could enhance its binding with the negatively charged MA-vacancy (*13*). Indeed, the E_{int} values were -0.74, -0.89, -0.92, and -1.22 eV for An, 4FAn, 26FAn, 345FAn, respectively (Fig. 3Ee), indicating that 345FAn exhibited the strongest interaction with the perovskite surface. It is also noted that future computational studies could beneficially predict the binding energy of the N 1s XPS peak to further understand ligand interactions.

Perovskite degradation and solar cell studies

We used TR and TOF-SIMS to study perovskite degradation. The TR results indicated that PEA-based 2D perovskites were thermally unstable on the film surface and decomposed into PbI_2 after thermal aging at 85°C for 2 hours (Fig. 4, A and B). This process we associated with the diffusion of PEA cations into bulk perovskites, as was seen in TOF-SIMS (Fig. 4C) and AR-XPS (fig. S13). The dynamic nature of 2D/3D heterostructures was also confirmed for BA, OA, DA, and 3FPEA (fig. S14). In contrast, neither ligand penetration nor phase degradation was observed for An- and 345FAn-treated films (Fig. 4C and fig. S15). These results suggested that suppressing ligand intercalation into 3D perovskites led to improved interface stability under thermal stress.

We monitored the photoluminescence (PL) stability of perovskite films after annealing at 85°C (Fig. 4D). The emission intensity of the untreated control and PEA-treated films degraded to 30% of its initial value within 144 hours (Fig. 4E), as seen in the previous reports (*31*). In contrast, An- and 345FAn-treated films show improved thermal stability, and 345FAn-treated perovskites retained 85% of their initial brightness following annealing.

We fabricated inverted-structure PSCs to investigate how ammonium ligands influenced the efficiency and stability of PSCs. We used both $Cs_{0.05}MA_{0.05}FA_{0.9}Pb(I_{0.95}Br_{0.05})_3$ and $Cs_{0.05}MA_{0.15}FA_{0.8}PbI_3$ perovskites as the absorber, the self-assembled monolayer 2PACz as the

hole transport layer (HTL), the thermally evaporated C_{60}/BCP bilayer as the electron transport layer (ETL), and indium tin oxide (ITO) as the transparent electrode (see Methods). Three representative ammonium ligands, including the 2D-forming PEA cation and the non-invasive An and 345FAn cations, were used for interfacial engineering. The cross-sectional SEM image of a complete device is shown in fig. S16.

Device performance (Fig. 5A) showed that compared to control devices, PEA-treated $Cs_{0.05}MA_{0.15}FA_{0.8}PbI_3$ PSCs (16 devices) provided improved PV performance with an average PCE of 23.2% (Fig. 5A and fig. S17). The average PCE of An devices decreased to 19.9%, a finding we linked to perovskite decomposition. Because of the improved surface passivation, 345FAn treatment increased average PCEs of $Cs_{0.05}MA_{0.15}FA_{0.8}PbI_3$ and $Cs_{0.05}MA_{0.05}FA_{0.9}Pb(I_{0.95}Br_{0.05})_3$ PSCs to 23.3% and 22.9%, respectively (Fig. 5A and fig. S18). The external quantum efficiency (EQE) spectra of the champion cells (Fig. 5B) for PEA and 345FAn devices exhibited improved charge collection compared to controls, and their integrated J_{sc} values matched well with those from the current-voltage (I-V) sweep.

We sent a 345FAn-treated $Cs_{0.05}MA_{0.15}FA_{0.8}PbI_3$ device to National Renewable Energy Laboratory (NREL, USA) for independent characterization. The device delivered a certified PCE of 24.09% using a quasi-steady-state (QSS) I-V sweep (Fig. 5C and fig. S19). The QSS-certified efficiency reported for inverted PSCs is compared to that of other devices in Table S2.

Seeking better to understand the improved performance, we used ultraviolet photoelectron spectroscopy (UPS) to characterize the electronic structure of the perovskite films. The secondary electron cut-off spectra (fig. S20) showed that 345FAn decreased the work function of perovskites from 4.64 to 4.17 eV and shifted the valence band maximum from 1.15 eV below the Fermi level in the control perovskites to 1.50 eV below the Fermi level. Taken together, these results show that 345FAn induced more n-type character in the perovskite film (fig. S20), which in inverted PSCs leads to favorable band bending for electron extraction and a decrease in non-radiative carrier recombination (*44*, *45*).

We performed optoelectronic characterization to investigate carrier recombination. From photoluminescence quantum yield (PLQY) measurements, we identify nonradiative recombination at the perovskite/C_{60} interface as the limiting factor for the performance of control devices (fig. S21). This recombination loss corresponded to a reduction of the quasi-Fermi level splitting (QFLS) by ~100 meV (table S3) (*46*, *47*). We found PEA and 345FAn passivation could reduce the interfacial nonradiative recombination, as reflected from the improved QFLS relative to the control stack by ~15 and ~30 meV, respectively. We further analyzed the energy loss of PSCs based on the device diode characteristics (figs. S22 and S23) (*48*). Consistent with the PL studies, nonradiative losses are reduced for PEA and 345FAn devices (12.7% and 12.1% for PEA and 345FAn, respectively), compared to those of the control device (16.5%) (fig. S24).

We evaluated the impact of ligand reactivity on the material processing of PSCs. We varied the solution exposure time between 0 s (dynamic spinning) and 120 s and tracked the PV parameters of PSCs accordingly (Fig. 5D and fig. S25). The average PCE of PEA devices (8 devices for each condition) dropped to 15.8%, with an average fill factor (FF) of merely 67.4% over the course of solution exposure for 30 s, while 345FAn devices maintained an average PCE of 23.0% (Fig. 5d). Wide solution-processing windows were also achieved for other non-penetrating ligands, such as 35tbuAn, 4FAn, and 26FAn (fig. S26). In pursuit of initial evidence of capacity to scale area, we fabricated perovskite solar modules (PSMs) with an active area of 22 cm^2 and 9 interconnected subcells (Methods). The champion PCE under reverse voltage scan was improved from 19.9% to 20.8% for the 345FAn-treated PSMs, with a V_{oc} of 10.13 V, an FF of 74.2%, and a J_{sc} of 2.77 mA cm^{-2} (fig. S27).

We studied the operating stability of PSCs using ISOS protocols (*49*). Accelerated lifetime testing was performed at the ISOS-L-3-85°C level, which constitutes light-soaking tests at 50% RH and 85°C with maximum power point (MPP) tracking. We used atomic-layer deposition for SnO_2 as the buffer layer and $Cs_{0.05}MA_{0.05}FA_{0.9}Pb(I_{0.95}Br_{0.05})_3$ perovskites as the absorber (see Methods). The initial PCEs of the encapsulated control, PEA, and 345FAn devices were 18.9%, 20.1%, and 20.2%, respectively (fig. S28). The stability results are shown in Fig. 5E. We recorded a similar T_{80} of ~220 hours for the control and PEA devices, in accordance with the limited thermal stability of perovskite films (Fig. 3E). We found that 2D/3D PSCs based on alkyl ammonium BA and OA were even less stable than the control device (fig. S29), whereas the 345FAn device retained >80% of its initial value after the 800-hour test. We estimate the T_{80} of 810 h for the 345FAn device (fig. S30), representing a fourfold enhancement over the operating lifetime of the PEA device.

To improve the T_{80} further, we moved to fluorine-doped tin oxide (FTO) as an alternative transparent electrode (fig. S31) in light of its chemical stability (*50*, *51*). We monitored the MPP of the encapsulated device under 1-sun illumination at 50% RH and 85°C. The initial PCE was 19.0%, which increased progressively to a peak value of 19.9% after ~ 50 hours of operation (Fig. 5F). This maximum efficiency (PCE_{max}) corresponds to a temperature coefficient of -0.12% /°C relative to the room-temperature device PCE (21.5%), which is consistent with reported results for inverted PSCs (*52*). After 1586 hours of continuous operation, the PCE dropped to 16.8% (84% of the PCE_{max}), mostly because of a reduction in current density (Fig. 5G). We determined the T_{85} to be ~1560 h (Fig. 5F). A comparison with other ISOS-L-3-stable PSCs is provided in Table S4.

Discussion

Two types of 2D/3D heterostructures have been reported for ISOS-L-3-stable PSCs: 3FPEA-intercalated 2D/3D perovskites (*23*) and all-inorganic heterostructures (*12*). For all-inorganic PSCs, the T_{85} reached an impressive 4000 h at 85°C, but with further room for progress in PCE (<= 17% when measured at 85°C). 3FPEA-based PSCs have achieved PCEs exceeding 23% at room temperature, but stable operation over 500 hours was limited to 65°C.

Aided by spectroscopic techniques, including AR-XPS, TOF-SIMS, and TR, we see evidence herein that certain 2D/3D heterostructures, such as those employing typical ammonium ligands such as PEA, 3FPEA, BA, and OA, may evince thermal degradation, something we assign to the dynamic nature of the interfaces at elevated temperatures. Anilinium and its fluorinated derivatives offer a more robust interface structure, correlated with limited penetration into the bulk of perovskites. Fluorinated An contributed interface passivation linked to strong interactions with perovskite surfaces. The resultant optimized 345FAn devices are among the most stable PSCs seen under ISOS-L-3 protocols at 85°C, achieving PCE of 19.9% during MPP tracking at this elevated operating temperature.

References and Notes

1. N. M. Haegel *et al.*, Terawatt-scale photovoltaics: Transform global energy. *Science*. **364**, 836–838 (2019).
2. National Renewable Energy Laboratory, Best research-cell efficiencies, (available at https://www.nrel.gov/pv/cell-efficiency.html).
3. H. Min *et al.*, Perovskite solar cells with atomically coherent interlayers on SnO2 electrodes. *Nature*. **598**, 444–450 (2021).
4. M. Kim *et al.*, Conformal quantum dot–SnO 2 layers as electron transporters for efficient perovskite solar cells. *Science*. **375**, 302–306 (2022).
5. J. Jeong *et al.*, Pseudo-halide anion engineering for α-FAPbI3 perovskite solar cells. *Nature*. **592**, 381–385 (2021).
6. Z. Song *et al.*, A technoeconomic analysis of perovskite solar module manufacturing with low-cost materials and techniques. *Energy Environ. Sci.* **10**, 1297–1305 (2017).
7. Y. Zhao *et al.*, A bilayer conducting polymer structure for planar perovskite solar cells with over 1,400 hours operational stability at elevated temperatures. *Nat. Energy*. **7**, 144–152 (2022).
8. S. Bai *et al.*, Planar perovskite solar cells with long-term stability using ionic liquid additives. *Nature*. **571**, 245–250 (2019).
9. Q. Cao *et al.*, Efficient and stable inverted perovskite solar cells with very high fill factors via incorporation of star-shaped polymer. *Sci. Adv.* **7**, 1–12 (2021).
10. Y. Liu *et al.*, Stabilization of Highly Efficient and Stable Phase-Pure FAPbI 3 Perovskite Solar Cells by Molecularly Tailored 2D-Overlayers. *Angew. Chemie Int. Ed.* **59**, 15688–15694 (2020).
11. Y.-H. Lin *et al.*, A piperidinium salt stabilizes efficient metal-halide perovskite solar cells. *Science*. **369**, 96–102 (2020).
12. X. Zhao *et al.*, Accelerated aging of all-inorganic, interface-stabilized perovskite solar cells. *Science*. **377**, 307–310 (2022).
13. R. Lin *et al.*, All-perovskite tandem solar cells with improved grain surface passivation. *Nature*. **603**, 73–78 (2022).
14. X. Li *et al.*, Constructing heterojunctions by surface sulfidation for efficient inverted

perovskite solar cells. *Science*. **375**, 434–437 (2022).

15. L. Chao *et al.*, Origin of High Efficiency and Long-Term Stability in Ionic Liquid Perovskite Photovoltaic. *Research*. **2020**, 1–13 (2020).
16. H. Kim *et al.*, Proton-transfer-induced 3D/2D hybrid perovskites suppress ion migration and reduce luminance overshoot. *Nat. Commun.* **11**, 3378 (2020).
17. H. Zhu *et al.*, Tailored Amphiphilic Molecular Mitigators for Stable Perovskite Solar Cells with 23.5% Efficiency. *Adv. Mater.* **32**, 1907757 (2020).
18. S. Yang *et al.*, Stabilizing halide perovskite surfaces for solar cell operation with wide-bandgap lead oxysalts. *Science*. **365**, 473–478 (2019).
19. J. Warby *et al.*, Understanding Performance Limiting Interfacial Recombination in pin Perovskite Solar Cells. *Adv. Energy Mater.* **2103567**, 2103567 (2022).
20. S. M. Park, A. Abtahi, A. M. Boehm, K. R. Graham, Surface Ligands for Methylammonium Lead Iodide Films: Surface Coverage, Energetics, and Photovoltaic Performance. *ACS Energy Lett.* **5**, 799–806 (2020).
21. J. J. Yoo *et al.*, An interface stabilized perovskite solar cell with high stabilized efficiency and low voltage loss. *Energy Environ. Sci.* **12**, 2192–2199 (2019).
22. J. J. Yoo *et al.*, Efficient perovskite solar cells via improved carrier management. *Nature*. **590**, 587–593 (2021).
23. H. Chen *et al.*, Quantum-size-tuned heterostructures enable efficient and stable inverted perovskite solar cells. *Nat. Photonics*. **16**, 352–358 (2022).
24. A. H. Proppe *et al.*, Multication perovskite 2D/3D interfaces form via progressive dimensional reduction. *Nat. Commun.* **12**, 3472 (2021).
25. S. Sidhik *et al.*, Deterministic fabrication of 3D/2D perovskite bilayer stacks for durable and efficient solar cells. *Science*. **377**, 1425–1430 (2022).
26. Y. Liu *et al.*, Ultrahydrophobic 3D/2D fluoroarene bilayer-based water-resistant perovskite solar cells with efficiencies exceeding 22%. *Sci. Adv.* **5**, eaaw2543 (2019).
27. J. Chakkamalayath, N. Hiott, P. V. Kamat, How Stable Is the 2D/3D Interface of Metal Halide Perovskite under Light and Heat? *ACS Energy Lett.* **8**, 169–171 (2023).
28. C. A. R. Perini *et al.*, Interface Reconstruction from Ruddlesden–Popper Structures Impacts Stability in Lead Halide Perovskite Solar Cells. *Adv. Mater.* **34**, 2204726 (2022).
29. A. A. Sutanto *et al.*, In Situ Analysis Reveals the Role of 2D Perovskite in Preventing Thermal-Induced Degradation in 2D/3D Perovskite Interfaces. *Nano Lett.* **20**, 3992–3998 (2020).
30. R. Azmi *et al.*, Damp heat–stable perovskite solar cells with tailored-dimensionality 2D/3D heterojunctions. *Science*. **376**, 73–77 (2022).
31. Q. Jiang *et al.*, Surface passivation of perovskite film for efficient solar cells. *Nat. Photonics*. **13**, 460–466 (2019).
32. C. Liu *et al.*, Tuning structural isomers of phenylenediammonium to afford efficient and stable perovskite solar cells and modules. *Nat. Commun.* **12**, 6394 (2021).

33. S. Kumar, L. Houben, K. Rechav, D. Cahen, Halide perovskite dynamics at work : Large cations at 2D-on-3D interfaces are mobile. *PNAS*. **119**, 1–9 (2022).

34. M. M. Tavakoli *et al.*, Addition of adamantylammonium iodide to hole transport layers enables highly efficient and electroluminescent perovskite solar cells. *Energy Environ. Sci.* **11**, 3310–3320 (2018).

35. S.-H. Lee *et al.*, Acid Dissociation Constant: A Criterion for Selecting Passivation Agents in Perovskite Solar Cells. *ACS Energy Lett.* **6**, 1612–1621 (2021).

36. C. S. Fadley, Angle-resolved x-ray photoelectron spectroscopy. *Prog. Surf. Sci.* **16**, 275–388 (1984).

37. B. Lv, T. Qian, H. Ding, Angle-resolved photoemission spectroscopy and its application to topological materials. *Nat. Rev. Phys.* **1**, 609–626 (2019).

38. Y. Wei *et al.*, Reverse-Graded 2D Ruddlesden–Popper Perovskites for Efficient Air-Stable Solar Cells. *Adv. Energy Mater.* **9**, 1900612 (2019).

39. D. Bi *et al.*, Multifunctional molecular modulators for perovskite solar cells with over 20% efficiency and high operational stability. *Nat. Commun.* **9**, 4482 (2018).

40. Y. Liu *et al.*, Ultrahydrophobic 3D/2D fluoroarene bilayer-based water-resistant perovskite solar cells with efficiencies exceeding 22%. *Sci. Adv.* **5**, 1–9 (2019).

41. M. A. Hope *et al.*, Nanoscale Phase Segregation in Supramolecular π - Templating for Hybrid Perovskite Photovoltaics from NMR Crystallography. *J. Am. Chem. Soc*. **143**, 1529–1538 (2021).

42. Y. Yang *et al.*, Top and bottom surfaces limit carrier lifetime in lead iodide perovskite films. *Nat. Energy*. **2**, 16207 (2017).

43. R. Lyu, C. E. Moore, T. Liu, Y. Yu, Y. Wu, Predictive Design Model for Low-Dimensional Organic–Inorganic Halide Perovskites Assisted by Machine Learning. *J. Am. Chem. Soc.* **143**, 12766–12776 (2021).

44. D. Luo *et al.*, Enhanced photovoltage for inverted planar heterojunction perovskite solar cells. *Science*. **360**, 1442–1446 (2018).

45. Q. Jiang *et al.*, Surface reaction for efficient and stable inverted perovskite solar cells. *Nature*. **611**, 278–283 (2022).

46. M. Stolterfoht *et al.*, How To Quantify the Efficiency Potential of Neat Perovskite Films: Perovskite Semiconductors with an Implied Efficiency Exceeding 28%. *Adv. Mater.* **32**, 2000080 (2020).

47. M. Stolterfoht *et al.*, Visualization and suppression of interfacial recombination for high-efficiency large-area pin perovskite solar cells. *Nat. Energy*. **3**, 847–854 (2018).

48. H. Zhang *et al.*, Multimodal host–guest complexation for efficient and stable perovskite photovoltaics. *Nat. Commun.* **12**, 3383 (2021).

49. M. V. Khenkin *et al.*, Consensus statement for stability assessment and reporting for perovskite photovoltaics based on ISOS procedures. *Nat. Energy*. **5**, 35–49 (2020).

50. J. D. Benck, B. A. Pinaud, Y. Gorlin, T. F. Jaramillo, Substrate Selection for Fundamental Studies of Electrocatalysts and Photoelectrodes: Inert Potential Windows in Acidic,

Neutral, and Basic Electrolyte. *PLoS One*. **9**, e107942 (2014).

51. R. A. Kerner, B. P. Rand, Electrochemical and Thermal Etching of Indium Tin Oxide by Solid-State Hybrid Organic–Inorganic Perovskites. *ACS Appl. Energy Mater.* **2**, 6097–6101 (2019).
52. T. Moot *et al.*, Temperature Coefficients of Perovskite Photovoltaics for Energy Yield Calculations. *ACS Energy Lett.* **6**, 2038–2047 (2021).
53. S. P. Harvey *et al.*, Mitigating Measurement Artifacts in TOF-SIMS Analysis of Perovskite Solar Cells. *ACS Appl. Mater. Interfaces*. **11**, 30911–30918 (2019).
54. R. A. Vargas−Hernández, Bayesian Optimization for Calibrating and Selecting Hybrid-Density Functional Models. *J. Phys. Chem. A*. **124**, 4053–4061 (2020).
55. J. P. Perdew, K. Burke, M. Ernzerhof, Generalized Gradient Approximation Made Simple. *Phys. Rev. Lett.* **77**, 3865–3868 (1996).
56. K. Lee, É. D. Murray, L. Kong, B. I. Lundqvist, D. C. Langreth, Higher-accuracy van der Waals density functional. *Phys. Rev. B*. **82**, 081101 (2010).
57. T. Lu, F. Chen, Multiwfn: A multifunctional wavefunction analyzer. *J. Comput. Chem.* **33**, 580–592 (2012).
58. J. Endres *et al.*, Valence and Conduction Band Densities of States of Metal Halide Perovskites: A Combined Experimental–Theoretical Study. *J. Phys. Chem. Lett.* **7**, 2722–2729 (2016).
59. P. Caprioglio *et al.*, On the Origin of the Ideality Factor in Perovskite Solar Cells. *Adv. Energy Mater.* **10**, 2000502 (2020).
60. W. Tress *et al.*, Interpretation and evolution of open-circuit voltage, recombination, ideality factor and subgap defect states during reversible light-soaking and irreversible degradation of perovskite solar cells. *Energy Environ. Sci.* **11**, 151–165 (2018).
61. A. Castro-Chong *et al.*, Illumination Intensity Dependence of the Recombination Mechanism in Mixed Perovskite Solar Cells. *Chempluschem*. **86**, 1347–1356 (2021).
62. S. Chen, X. Xiao, H. Gu, J. Huang, Iodine reduction for reproducible and high-performance perovskite solar cells and modules. *Sci. Adv.* **7**, 1–7 (2021).
63. X. Zheng *et al.*, Managing grains and interfaces via ligand anchoring enables 22.3%-efficiency inverted perovskite solar cells. *Nat. Energy*. **5**, 131–140 (2020).

Acknowledgements: Funding: This research was made possible by the U.S. Department of the Navy, Office of Naval Research Grant (N00014-20-1-2572). This work was supported in part by Ontario Research Fund-Research Excellence program (ORF7-Ministry of Research and Innovation, Ontario Research Fund-Research Excellence Round 7). This work was also supported under award number OSR-CRG2020-4350.2. S.M.P., H.R.A., and K.R.G. gratefully acknowledge the U.S. Department of Energy, Office of Science, Office of Basic Energy Sciences, and the EPSCoR program, under award no. DE-SC0018208 for XPS measurements. K.R.R., Z.C., J.T.P., C.M.R., and K.R.G. acknowledge funding from the National Science Foundation through

Cooperative Agreement Number 1849213. Supercomputing resources on the Lipscomb High Performance Computing Cluster were provided by the University of Kentucky Information Technology Department and Center for Computational Sciences (CCS). M.W. acknowledges funding from the European Union's Horizon 2020 Research and Innovation program under the Marie Skłodowska-Curie Grant Agreement No. 101026353. TW and AA acknowledge the support of the National Science Foundation under award number ECCS-1936527. AA acknowledges partial support by the Office of Naval Research under award number N00014-20-1-2573. This work made use of the NUFAB and Keck-II facilities of Northwestern University's NUANCE Center, which has received support from the SHyNE Resource (NSF ECCS-2025633), the IIN, and Northwestern's MRSEC program (NSF DMR-1720139).

Author contributions: S.M.P., M.W., K.R.G., M.G., and E.H.S. conceived the idea and proposed the experimental and modeling design. S.M.P. and M.W. fabricated all the devices and conducted the characterization. S.M.P and H.R.A performed XPS and UPS characterization and data analysis. J.X., K.R.R., and C.M.R. carried out the DFT simulation. Y.Y., C.L., and M.G.K. measured TOF-SIMS and fabricated PSMs. F.T.E., M.W., S.M.Z., and M.G. conducted the PL characterization and data analysis. K.D., T.W., and A.A. performed the GIWAXS measurements. S.T. and S.M.P. measured the TR spectra. L.G., B.C, H.C., L.Z., A.M., and Z.W helped with the device fabrication and material characterization. Z.C. and J.T.P. performed the contact-angle measurements. M.W., S.M.P., J.X., K.R.G, M.G., and E.H.S. co-wrote the manuscript. All authors contributed to data analysis, read and commented on the manuscript.

Competing interests: The authors declare no competing interests.

Data and materials availability: All data are provided in the main text or the supplementary materials.

Supplementary Materials

Materials and Methods

Supplementary Text

Figs. S1 to S31

Tables S1 to S4

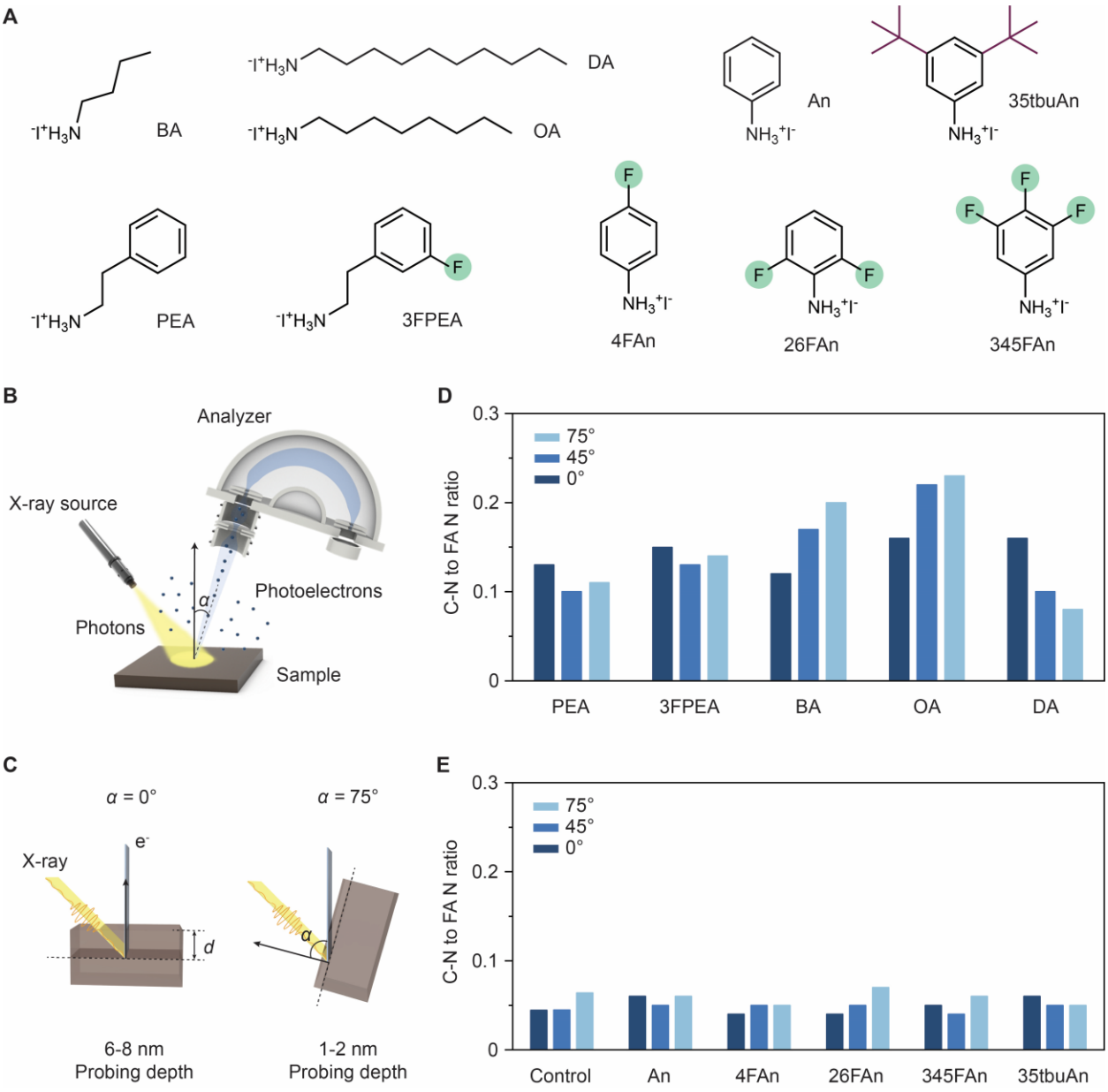

Fig. 1. AR-XPS characterization of ammonium ligand penetration. (**A**) Chemical structures of the ammonium ligands investigated in this study. (**B**) Experimental setup for AR-XPS characterization. The electron take-off angle α is defined as the angle between the normal of the sample substrate and the analyzer. (**C**) Schematic indicating the relation between α and the photoelectron probing depth d. (**D-E**) C-N to FA N ratios at electron take-off angles of 0°, 45°, and 75° for the control (untreated) and ammonium ligand-treated perovskite films. The results show reduced bulk and surface existence for An and An derivatives.

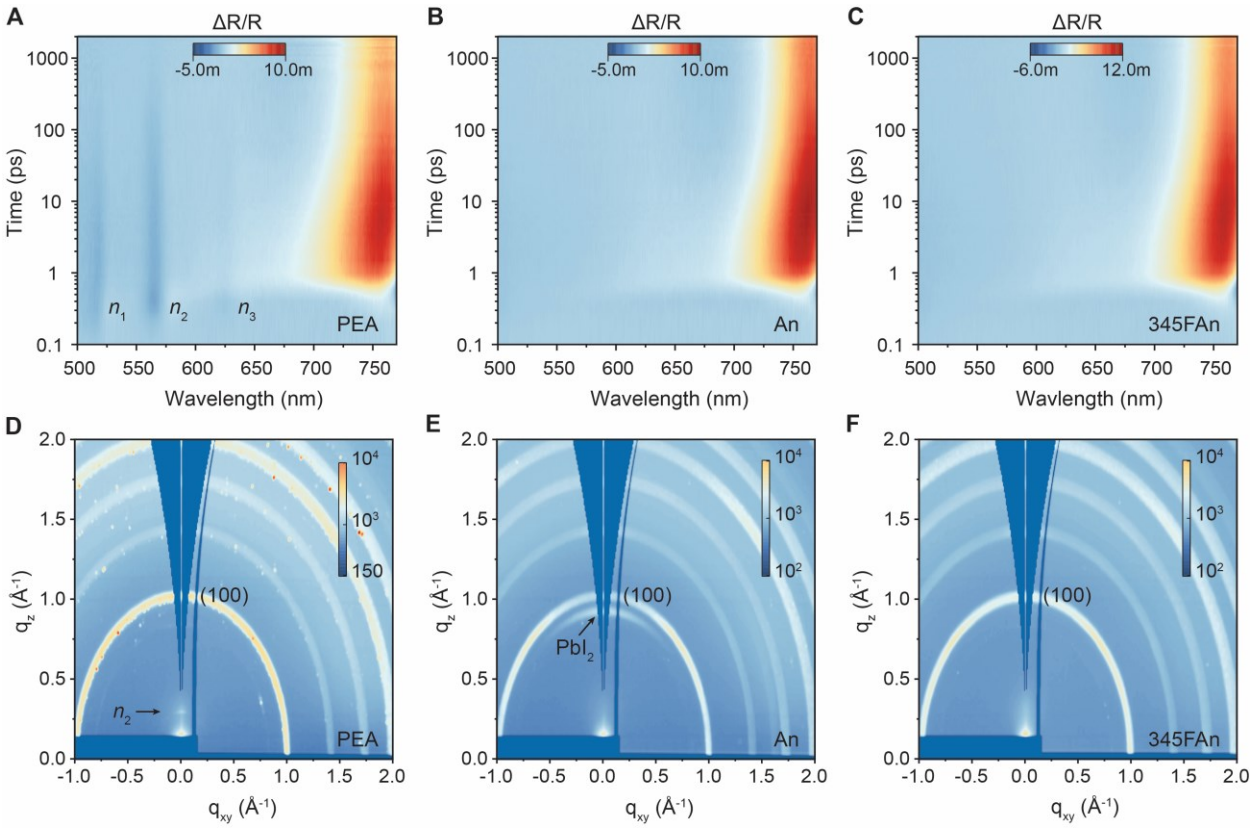

Fig. 2. Phase transformation of perovskite films. (**A-C**) Pseudocolor representation of the transient reflectance spectra for the PEA (**A**), An (**B**), and 345FAn (**C**) treated perovskite films, respectively. n = 1, n = 2, n = 3 2D perovskites (n_1, n_2, and n_3) appear in the film after PEA passivation. (**D-F**) GIWAXS image for perovskite films of PEA (**D**), An (**E**), and 345FAn (**F**) passivation, respectively. The color bar shows the diffraction intensity collected from the GIWAXS detector. q_{xy} and q_z represent in-plane and near out-of-plane scattering vectors, respectively. n = 2 2D perovskite (n_2) and PbI_2 related diffraction peaks are observed in the PEA and An treated films, respectively. (100) refers to the (100) diffraction peak of 3D perovskites.

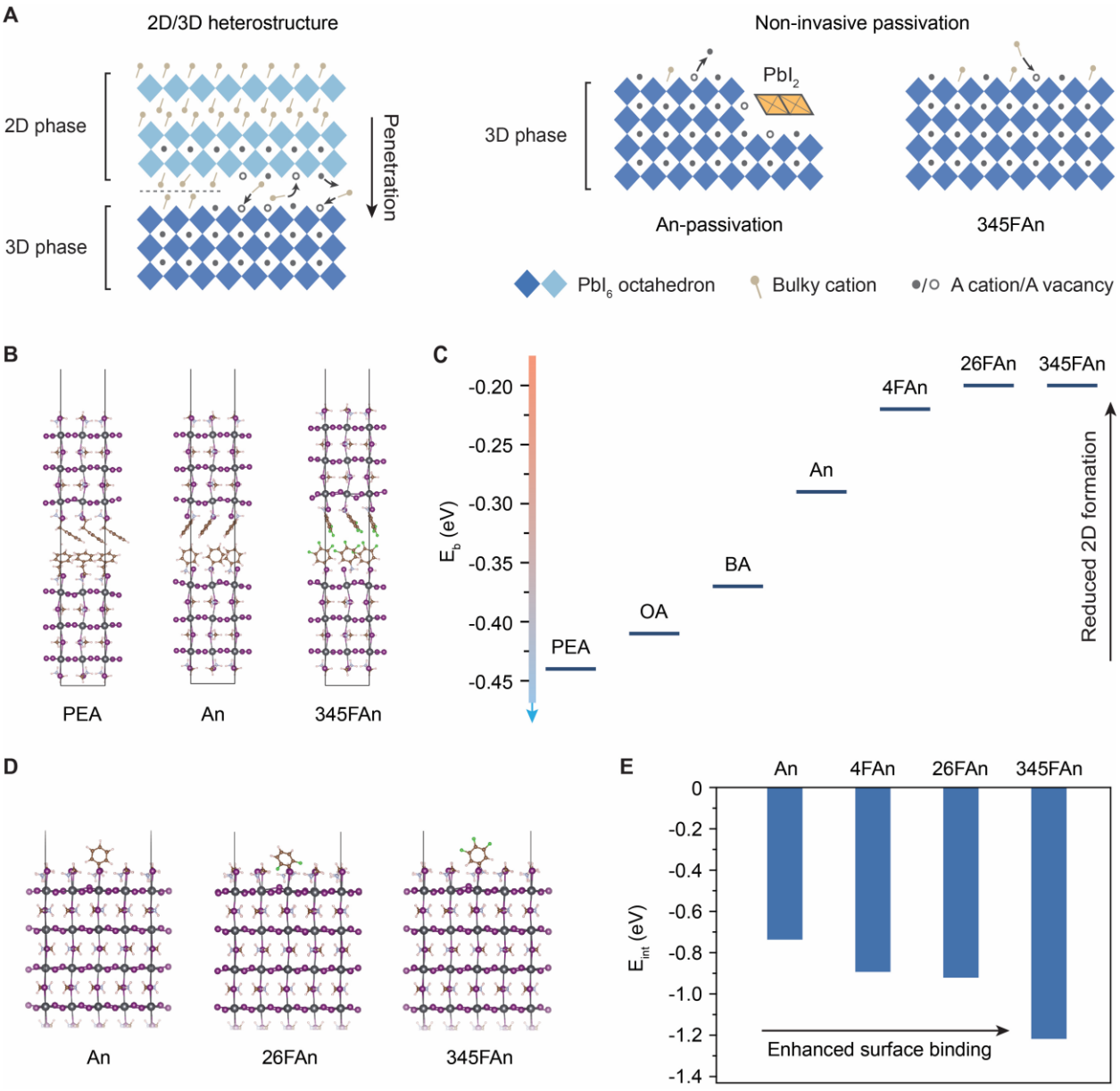

Fig. 3. DFT studies. (**A**) Schematic depiction of the model of ammonium ligand and perovskite interactions. (**B**) Models used in DFT calculations to calculate the binding energy (E_b) of adjacent 2D perovskite fragments. (**C**) E_b values for seven ammonium ligands substituted into $MAPbI_3$ perovskite slabs. **(D)** Models used to calculate the interaction energy (E_{int}) of ammonium ligands with the $MAPbI_3$ perovskite surface. **(E)** E_{int} values of four ammonium ligands with the perovskite surface.

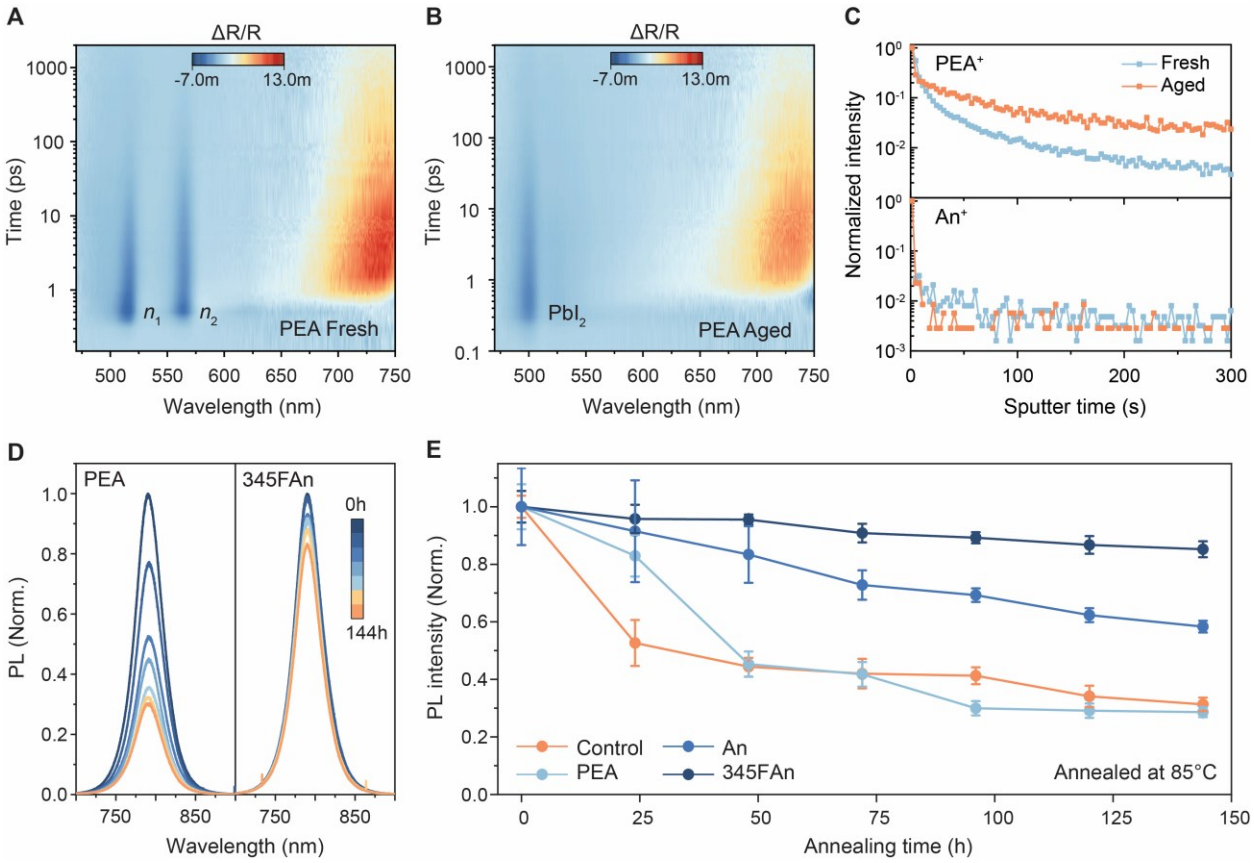

Fig. 4. Thermal stability of perovskite films. (**A-B**) Pseudocolor representation of the transient reflectance spectra for PEA-treated perovskite films before (**A**) and after (**B**) thermal ageing at 85°C for 2 h. 2D perovskites were decomposed into PbI_2 after thermal ageing. (**C**) The distribution of PEA^+ and An^+ in fresh and aged (at 85°C for 2 h) perovskite films using ToF-SIMS. (**D**) PL spectra of perovskite thin films under thermal annealing at 85°C. The films were kept on a hot plate at 85°C in the N_2-filled glovebox and measured every 24 h in ambient air. (**E**) Changes in PL intensity for different annealing times. Data are presented as mean values ± standard deviation. Three films were measured under each condition.

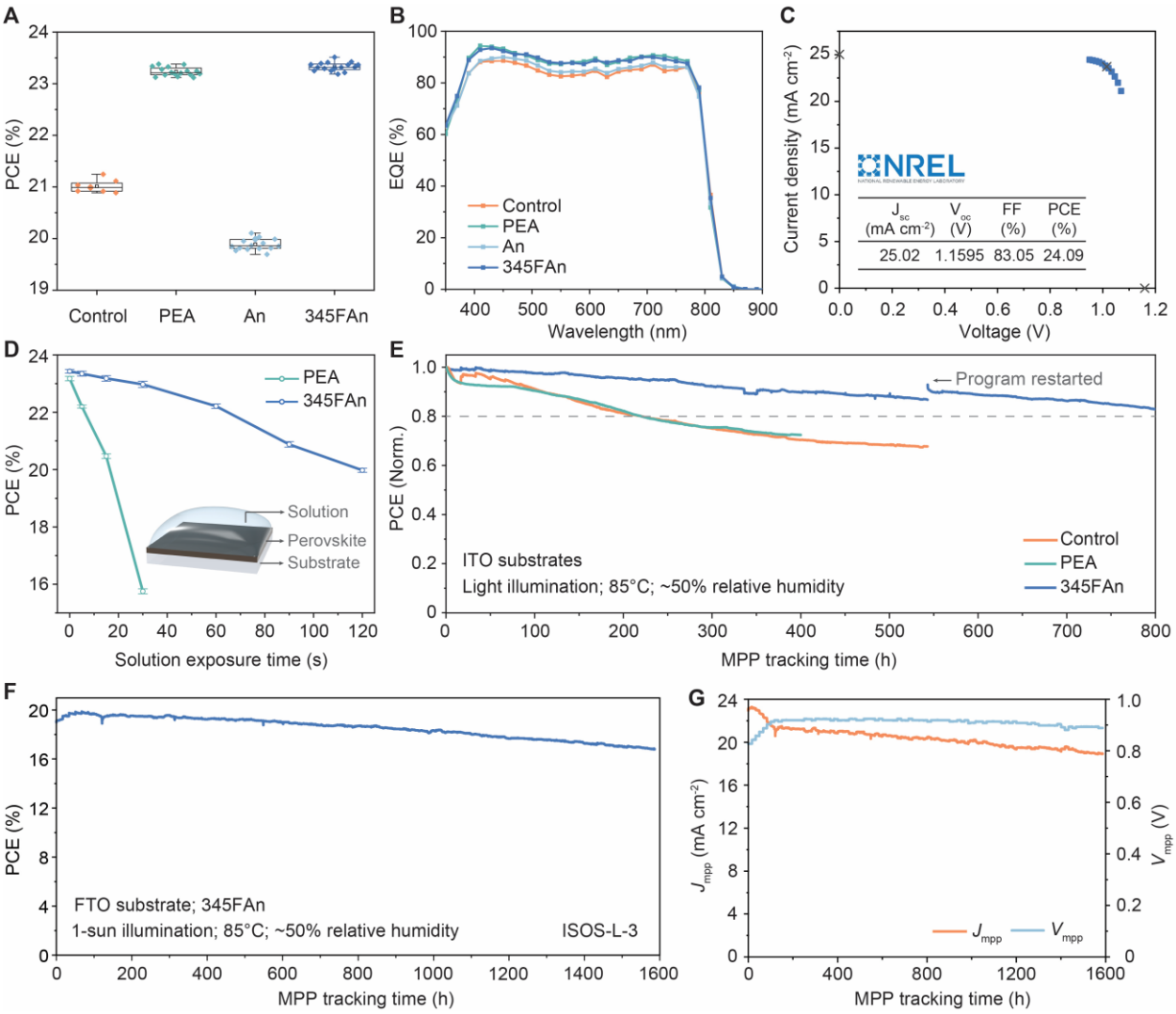

Fig. 5. Photovoltaic performance of PSCs with interface engineering. (**A**) PCE for control (8 devices) vs. ammonium ligand treated (16 devices for each type) PSCs. (**B**) EQE curves of the control and ammonium ligand treated devices. (**C**) Quasi-steady-state *J-V* curve of one representative 345FAn device certified at NREL. Inset: PV parameters of the device. (**D**) PCE evolution of PEA and 345FAn devices as a function of solution exposure time (8 devices for each condition). Data are presented as mean values ± standard deviation. The inset is a schematic illustration of the solution exposure process for interface engineering. (**E**) MPP tracking of encapsulated control, PEA, and 345FAn devices using ITO substrates at 85°C with a relative humidity of ~50% under 0.8-sun illumination. (**F-G**) PCE (**F**), current density (J_{mpp}), and voltage (V_{mpp}) (**G**) at the MPP of the encapsulated 345FAn device using a FTO substrate under 1-sun illumination at 85°C and ~50% relative humidity.

Science
AAAS

Supplementary Materials for

Engineering ligand reactivity enables high-temperature operation of stable perovskite solar cells

So Min Park, Mingyang Wei, Jian Xu, Harindi R. Atapattu, Felix T. Eickemeyer, Kasra Darabi, Luke Grater, Yi Yang, Cheng Liu, Sam Teale, Bin Chen, Hao Chen, Tonghui Wang, Lewei Zeng, Aidan Maxwell, Zaiwei Wang, Keerthan R. Rao, Zhuoyun Cai, Shaik M. Zakeeruddin, Jonathan T. Pham, Chad M. Risko, Aram Amassian, Mercouri G. Kanatzidis, Kenneth R. Graham, Michael Grätzel & Edward H. Sargent

Corresponding authors. E-mails: ted.sargent@utoronto.ca; michael.graetzel@epfl.ch; kenneth.graham@uky.edu

The PDF file includes:

Materials and Methods

Materials

All materials were used as received without further purification. Organic halide salts, including methylammonium iodide (MAI), formamidinium iodide (FAI), methylammonium bromide (MABr) methylammonium chloride (MACl), were purchased from Great Cell Solar, and cesium iodide (CsI) was purchased from Sigma-Aldrich. [2-(9H-Carbazol-9-yl)ethyl]phosphonic Acid (2PACz), lead iodide (PbI_2, 99.99%), and bathocuproine (BCP) were purchased from TCI. Anhydrous solvents including N, N-dimethylformamide (DMF, 99.8%), dimethyl sulfoxide (DMSO, 99.9%), 2-propanol (IPA, 99.5%), chloroform (CF, 99.8%), chlorobenzene (CB, 99.8%), and anisole (99.7%) were purchased from Sigma-Aldrich and toluene (99.8%) was purchased from Alfa Aesar. 3-fluoro-phenethylammonium iodide (3FPEAI) and C_{60} were purchased from Xi'an Polymer Light Technology Corp. Non-patterned indium tin oxide (ITO) coated glass substrates (15 Ω/sq) were purchased from Tinwell Technology. Commercial patterned ITO substrates (20 Ω/sq) with 25 mm x 25 mm dimensions were purchased from TFD Inc.

Bulky ammonium halide salts, including anilinium iodide (AnI, TCI, 98%), butylammonium iodide (BAI, TCI, 97%), phenethylammonium iodide (PEAI, Great Cell Solar, 99%), were purchased and used as received. 4-fluoroaniline (TCI, 98%), 2,6-difluoroaniline (TCI, 98%), 3,4,5-trifluoroaniline (TCI, 98%), octylamine (Alfa Aeser, 99%), decylamine (Sigma-Aldrich, 95%), and 3,5-di-tert-butylaniline (TCI, 98%) were purchased and converted to ammonium salts using the same procedure as reported before (*20*). The abbreviations of the converted ammonium salts are 4-fluoroanilinium iodide (4FAnI), 2,6-difluoroanilinium iodide (26FAnI), 3,4,5-trifluoroanilinium iodide (345FAnI), 3,5-di-tert-butylanilinium iodide (35tbuAnI), octylammonium iodide (OAI), and decylammonium iodide (DAI).

Perovskite film fabrication

The precursor solution (1.5 M) was prepared from CsI, MAI, FAI, $PbBr_2$, and PbI_2 precursors dissolved in mixed solvents of DMF and DMSO with a volume ratio of 4:1. For the $Cs_{0.05}MA_{0.15}FA_{0.8}PbI_3$ perovskite, the molar ratio for FAI/MAI/CsI was 0.8:0.15:0.05, and 10 mg mL^{-1} MACl was added in the solution to improve the film morphology; For the $Cs_{0.05}MA_{0.05}FA_{0.9}Pb(I_{0.95}Br_{0.05})_3$ perovskite, the molar ratios for FAI/MABr/CsI and $PbI_2/PbBr_2$ were 0.9:0.05:0.05 and 0.95:0.05, respectively. The precursor solution was filtered through a 0.22 μm polytetrafluoroethylene (PTFE) membrane before use. 60 μL of perovskite solution was deposited on the substrate and spun cast at 1000 rpm for 10 s followed by 6000 rpm for 30 s. 150 μL anisole was dropped onto the substrate during the last 5 s of the spinning, resulting in the formation of dark brown films that were then annealed on a hot plate at 100°C for 20 min.

Device fabrication

The pre-patterned ITO or FTO glasses were sequentially sonicated in aqueous detergent, deionized water, acetone, and IPA each for 10 min. After drying with nitrogen, the substrates were exposed to UV-ozone treatment for 15 min to remove organic contaminants. 100 μL of 2PACz in anhydrous ethanol (1 mmol/l) solution was spun-cast at 3000 rpm for 30 s inside the nitrogen-filled glovebox (<0.1 ppm of O_2 and H_2O) and annealed at 100°C for 10 min. Following the 2PACz coating, $Cs_{0.05}MA_{0.15}FA_{0.8}PbI_3$ perovskites were deposited on the substrate as detailed above. 200 μL of ammonium ligand solution (1mg/mL) in CF with an additional 3% of IPA was then drop cast within 2-3 s on the perovskite film spinning at 4000 rpm (i.e., dynamic spinning) and annealed at 100°C for 5 min. For the exposure time-dependent measurements, 200 μL of ammonium ligand solution was left on the perovskite film for a certain period before spinning at 4000 rpm. Both control and treated films were then transferred to the thermal evaporator (Angstrom engineering), and C_{60} (30 nm) and BCP (7 nm) were deposited sequentially with a rate of 0.3 Å/s and 0.5 Å/s, respectively, at a pressure of ca. 2 x 10^{-6} mbar. Finally, Ag contact (120 nm) was deposited on top of BCP through a shadow mask with the desired aperture area.

For the stability testing, $Cs_{0.05}MA_{0.05}FA_{0.9}Pb(I_{0.95}Br_{0.05})_3$ perovskites were instead deposited as described above, and C_{60} (30 nm) and ALD-SnO_2 were used as the electron transport layer. The deposition of ALD-SnO_2 was carried out in the PICOSUN R-200 Advanced ALD system. H_2O and TDMASn were used as oxygen and tin precursors. Precursor and substrate temperature were set to 75°C and 85°C, respectively. 90 SCCM N_2 was used as carrier gas. Pulse and purge times for H_2O were 1 s and 5 s, and 1.6 s and 5 s for TDMASn. The total deposition cycle is 150, corresponding to 20 nm of SnO_2.

Module Fabrication

Perovskite solar modules were fabricated on pre-cleaned FTO glass substrates with a size of 6 x 6 cm^2, which were patterned by a 1030 nm laser (LPKF ProtoLaser R) with nine sub-cells connected in series. FTO substrates were patterned with a laser power of 5 W (P1). The SnO_2 was used as the electron transport layer (ETL) using the chemical bath deposition method. The solution was prepared by adding 2.5 g of urea (Sigma-Aldrich, 99%), 3.5 mL of HCl (Sigma-Aldrich, 37% wt. % in water), 50 µL of thioglycolic acid (Sigma-Aldrich, 98%), and 0.55 g of $SnCl_2 \cdot 2H_2O$ (Sigma-Aldrich, 99.99%) into 200 mL of deionized water. The FTO substrates were immerged into the solution at 90°C for 5 hours, followed by annealing at 190°C for 1 hour. Then 1.5 M perovskite precursors with PbI_2 (TCI America, 99.99%): FAI (GreatCell Solar, 99.99%): MAI (GreatCell Solar, 99.99%): CsI (Sigma-Aldrich, 99.99%): MACl (GreatCell Solar, 99.99%) = 1: 0.85: 0.05: 0.05: 0.20) were dissolved in the mixed DMF (Sigma-Aldrich, 99.8%): DMSO (Sigma-Aldrich, 99.9%) = 4:1 (volume ratio) solvent. The perovskite films were deposited by spin-coating at 1000 rpm for 10 s and 5000 rpm for 30 s. At the 20 s of the second step, 200 µL of chlorobenzene (Sigma-Aldrich, 99.8%) was dropped onto the perovskite films to facilitate crystallization. The perovskite films were annealed at 100 °C for 10 min and 150 °C for 10 min. The passivation layer was fabricated by spinning 100 µL 345FAn solution (1 mg/mL) in isopropanol (Sigma-Aldrich, 99.5%) and chlorobenzene (1:1 volume ratio) at 5000 rpm 30s, followed by annealing at 100 °C for 10 min. The hole transport layer was deposited by spin-coating 0.06 M spiro-OMeTAD (Sigma-Aldrich, SHT-263 Solarpur) solution in chlorobenzene at 3000 rpm for 20 s. 0.03 M bis(trifluoromethanesulfonyl)-imide lithium salt (Sigma-Aldrich, 99.0%) in acetonitrile (Sigma-Aldrich, 99.8%), 0.2 M 4-tert-Butylpyridine (Sigma-Aldrich, 98%) and 0.0035 M FK 209 Co(III) TFSI salt (GreatCell Solar) in acetonitrile were added to the spiro-OMeTAD solution as additives. Then the P2 lines were patterned aligning with P1 using a laser power of 0.5 W. Finally, the electrode was realized by thermal evaporating a 70 nm gold under high vacuum, followed by P3 etching using a laser power of 0.5 W. The geometric fill factor (GFF) of 92% was defined as the active area (22.0 cm^2) divided by the aperture area (23.9 cm^2).

Solar cell characterization

The current-voltage (I-V) characteristics of solar cells were measured using a Keithley 2400 sourcemeter under the illumination of solar simulator (Newport, Class AAA) at the light intensity of 100 mW cm^{-2} as checked with a calibrated reference solar cell (Newport). Unless otherwise stated, the I-V curves were all measured in a nitrogen atmosphere with a scanning rate of 100 mV s^{-1} (voltage steps of 10 mV and a delay time of 100 ms). The active area was determined by the aperture shade mask (0.049 cm^2) placed in front of the solar cell to avoid overestimation of the photocurrent density. EQE measurements were performed using Newport system (QuantX-300) with monochromatic light and white bias light (~0.2 Sun). The system was calibrated by a certified silicon solar cell.

Stability tests of solar cells

Devices were placed in a homemade stability tracking station. The illumination source is a white light LED with intensity calibrated to match 0.8-sun conditions. For the ISOS-L-3 ageing protocol, the device chamber was left open in a room with 50±10% humidity and solar cell was mounted on a metal plate kept at 85°C by a heating element. A thermal couple attached to the metal plate was used to monitor and provide feedback control to the heating element to ensure temperature consistency. MPP was tracked using a home-build MATLAB-based MPP tracking system using a 'perturb and observe' method. The MPP was updated every 1000 minutes. Encapsulation was done by capping the device with a glass slide, using UV-adhesive (Lumtec LT-U001) as a sealant.

AR-XPS measurements

AR-XPS measurements were performed with a Thermo Scientific K-Alpha system with 180° double-focusing, hemispherical analyzer. The system is equipped with a 128-channel detector and monochromated small spot XPS. An Al Kα source (1486.6 eV) was used for excitation and a pass energy of 147.6 eV was used for XPS acquisition. Three electron take-off angles (α = 0°, 45°, and 75°) were defined as the angle between the normal of the perovskite sample and the analyzer (Fig. 1b). Samples mounted on a metal specimen holder were rotated along x, y, z directions to match the analyzing spots. All data were analyzed with Thermo Avantage software.

TR measurements

A regeneratively amplified Yb:KGW laser at a 5 kHz repetition rate (Light Conversion, Pharos) was used to generate femtosecond laser pulses, and a pulse picker was used to lower the frequency to 1 kHz. A portion of the 1,030 nm fundamental was sent into an optical bench (Ultrafast, Helios), where it passed through a retroreflector and was then focused into a calcium fluoride crystal, translated at 1 mm s^{-1}, to create the white light continuum probe. An optical parametric amplifier (Light Conversion, Orpheus) was used to generate the 450 nm pump pulse by upconversion of the fundamental wavelength. This was then sent to the optical bench and was chopped at 500 Hz. Both the pump and probe were sent to the sample, with the time delay adjusted by changing the path length of the probe (time resolution ~350 fs). The probe pulse was then collected by a CCD after dispersion by a grating spectrograph (Ultrafast). Time zero was allowed to vary with wavelength to account for the chirp of the probe.

GIWAXS measurements

GIWAXS measurements were performed at CMS beamline, NSLS II. The monochromatic X-ray with the energy of 13.5 keV shone upon the samples at different grazing incident angles of 0.08°, 0.12°, 0.25°, and 0.5° with an exposure time of 10 s. A Pilatus800K detector was placed 259 mm away from the sample to capture the 2D diffraction pattern.

PL and time-resolved PL (TRPL) measurements

Photoluminescence lifetime (TCSPC) was measured using an Edinburgh Instruments lifespec II fluorescence spectrometer; a picosecond pulse diode laser (EPL-510, excitation wavelength 510 nm, pulse width < 60 ps, fluence < 3 nJ cm^{-2}) was used. Absolute intensity photoluminescence spectra were measured using an integrating sphere, and Andor Kymera 193i spectrograph, and a 660 nm continuous-wave laser set at 1-Sun equivalent photon flux (1.1 μm beam full-width half-maximum, 632 μW); photoluminescence was collected at normal incidence using a 0.1 NA, 110 μm-diameter optical fiber.

TOF-SIMS Measurement

The time-of-flight secondary ion mass spectrometry (TOF-SIMS) measurements were performed on the IONTOF M6 instrument with a Bi^{3+} (30 keV) primary ion beam for analysis and an Ar-cluster gun (5 keV) for sputtering due to its low damage depth. Data was acquired for positive ions in an analysis area of 49 × 49 $μm^2$ centered inside the cluster raster area of 200 × 200 $μm^2$. No distribution gradient was observed for FA cations, indicating that measurement artifacts were successfully minimized (*53*).

Other characterizations

XRD spectra were collected with a Bruker-AXS D8 advance diffractometer with Cu Kα radiation (λ = 1.5418 Å) operating at 40 kV and 40 mA. Contact angles were measured with a standard goniometer (Ramé-hart) equipped with a camera was used to measure. A 4 μl drop of deionized water was placed onto the target surface and pictures were captured after 2 s of depositing the drop. The images were analyzed using ImageJ software to extract macroscale contact angle data. UPS measurements were taken with an Excitech H Lyman-α photon source (10.2 eV) with an oxygen-filled beam path coupled with the same PHI 5600 UHV and analyzer system. A sample bias of -5 V was applied and a pass energy of 5.85 eV was used for UPS acquisition. High-resolution SEM images were obtained using

the Hitachi S5200 microscope with an accelerating voltage of 1.5 kV. A low accelerating voltage and a low beam current were deployed to reduce surface damage of perovskite films under electron beam bombardment.

DFT calculations

First-principles calculations based on density functional theory (DFT) were carried out using the Vienna *Ab initio* Simulation Package (VASP) (*54*). The generalized gradient approximation (GGA) of Perdew-Burke-Ernzerhof (PBE) functional was employed as the exchange-correlation functional (*55*). We adopt DFT-D3 method for the van der Waals (vdW) correction (*56*). The plane-wave cutoff energy of 400 eV was used. The energy and force convergence criteria were set to 10^{-5} eV and 0.02 eV·Å $^{-1}$, respectively. In 2D perovskite formation calculations, the binding energies (E_b) of adjacent fragments was defined as (*24*): $E_B = E_{tot} - E_{fragment1} - E_{fragment2}$, where E_{tot}, $E_{fragment1}$ and $E_{fragment2}$ are the total energies of the entire system, and two fragments cut from the optimized system. The interaction energies (E_{int}) of different ammonium cations (L) with tetragonal $MAPbI_3$ perovskite surface were calculated as $E_{mol/pvsk} - E_{pvsk} - E_L$, where $E_{mol/pvsk}$, E_{pvsk} and E_L are the total energies of the adsorption system, the perovskite system and LI, respectively. We used a vacuum of 20 Å to separate two surfaces along the z-direction.

Supplementary Text

Analysis of the energy loss of PSCs

To elucidate the origin of energy loss in PSCs, we started by analyzing the device diode characteristics following our previously established procedure (*48*). We first obtained the ideality factor n of representative PSCs from the plots of their V_{oc}-incident light intensity dependence (fig. S16). Following these preparations, we break down the energy loss of PSCs based on the following procedures: (1) The Shockley-Queisser limit was calculated from bandgap which we determined from the PL peak wavelength of the perovskite thin film within a complete device stack (Fig. S15b). The bandgaps are found to be around 1.56 eV for different films with small variations. (2) The radiative limit is calculated by using the J_{sc} of the studied devices, the radiative limit of V_{oc}, and assuming an ideal diode behavior (n = 1; with series and shunt resistances of $R_{series} = 0$ and $R_{shunt} = \infty$, respectively). The performance losses related to the radiative limit with respect to the Shockley-Queisser limit account for 10.4% for the PEA device and 10.5% for the 345FAn device, mainly stemming from the non-ideal light absorption. (3) The contribution of non-radiative bulk and interface recombination (i.e., non-radiative losses) is further evaluated by calculating the transport limit using the measured V_{oc} and ideality factor, while maintaining the J_{sc} and ideal resistances. Comparing the transport limit with the radiative limit, non-radiative losses are found as 12.7% and 12.1% for PEA and 345FAn devices, respectively. (4) Finally, transport losses are analysed using the measured J-V curve with respect to the transport limit. The PEA device has a higher transport loss (7.4%) than that of 345FAn (6.2%).

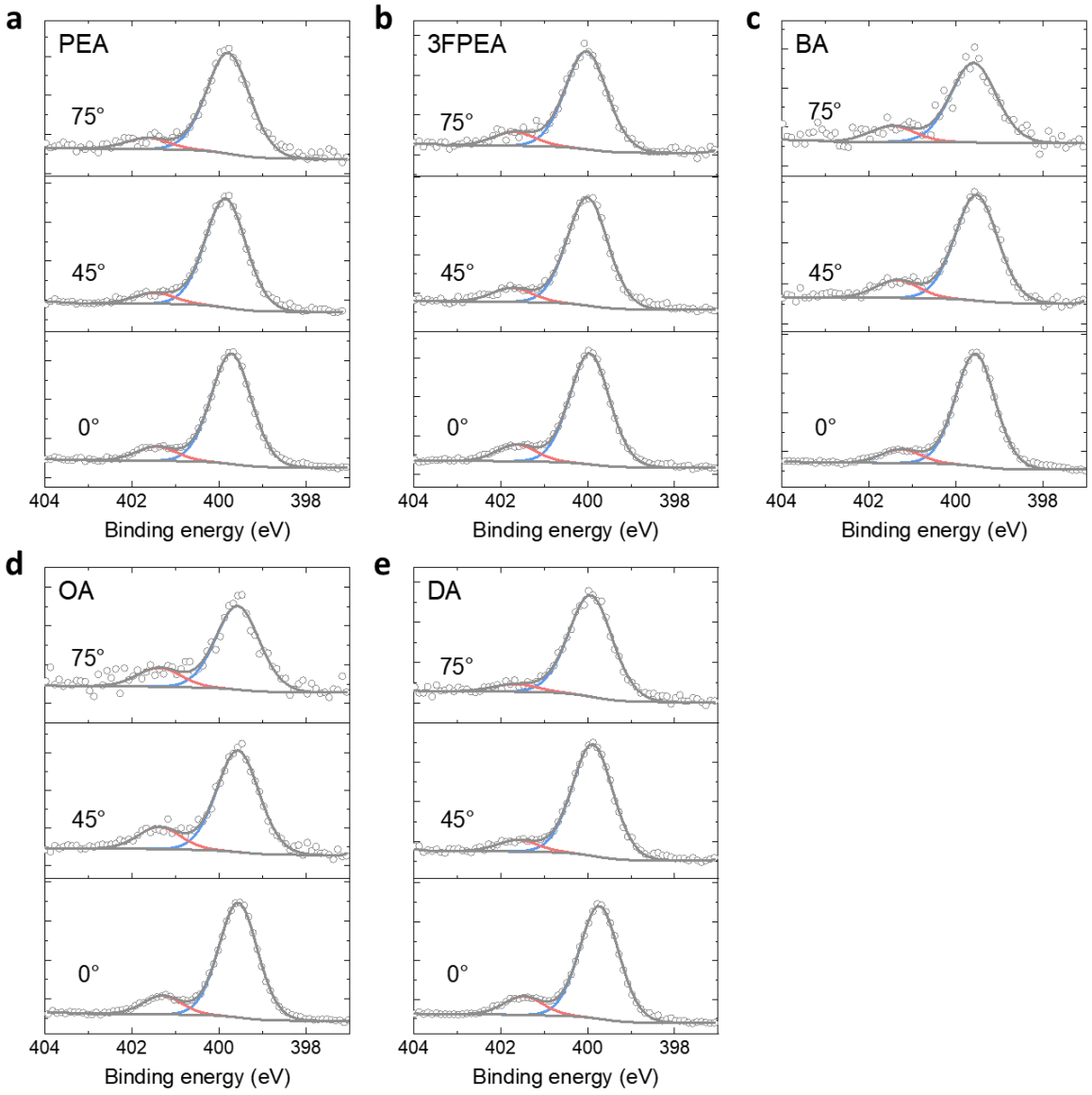

Fig. S1. AR-XPS N 1s region of perovskite films as a function of the electron take-off angles 0°, 45°, and 75°: **a-e,** PEA (**a**), 3FPEA (**b**), BA (**c**), OA (**d**), and DA (**e**) treated films. The pink peak fits the C-N bond and the blue to the N from FA.

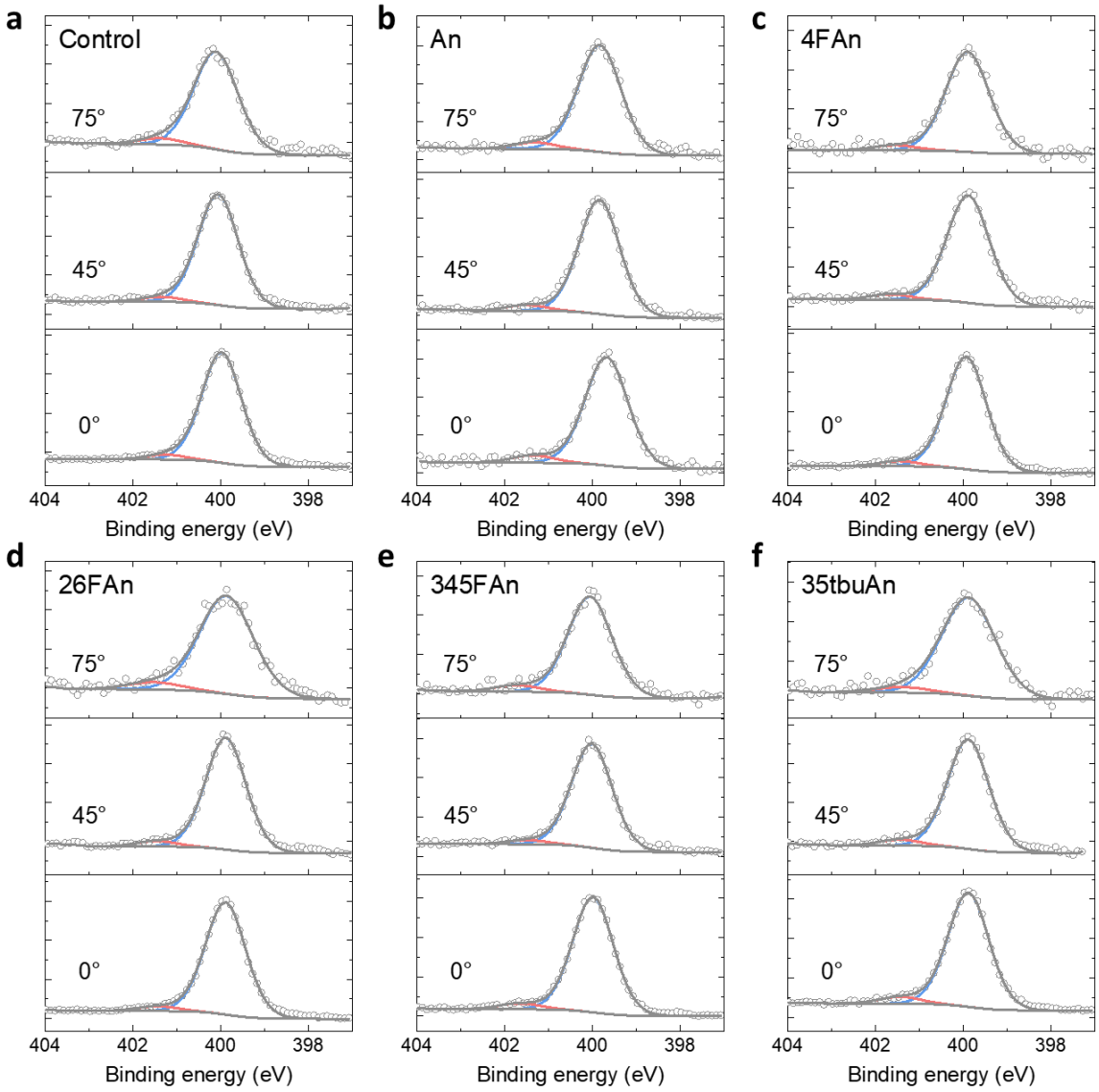

Fig. S2. AR-XPS N 1s region of An and An derivative treated perovskite films as a function of the electron take-off angles 0°, 45°, and 75°: **a-f,** control (**a**), An (**b**), 4FAn (**c**), 26FAn (**d**), 345FAn (**e**), and 35tbuAn (**f**) treated films. The pink peak fits the C-N bond and the blue to the N from FA.

5

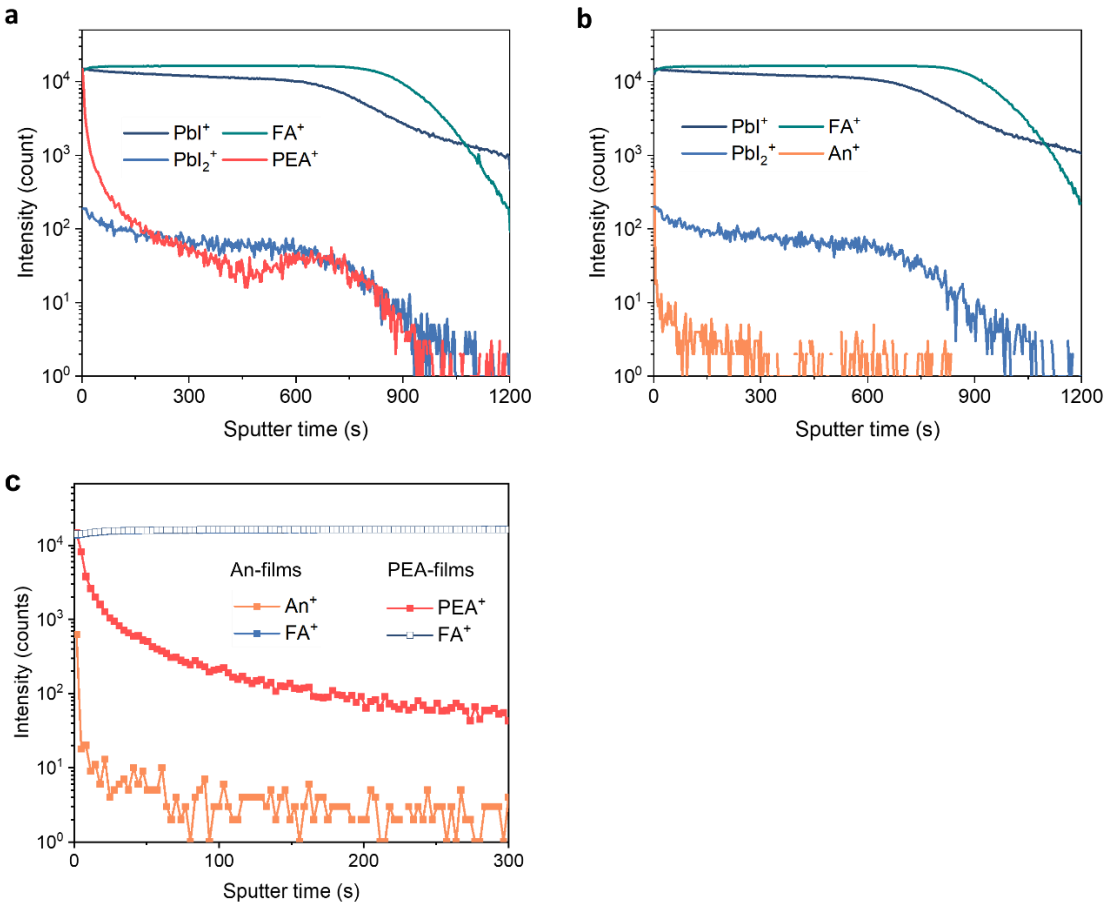

Fig. S3. a-b, TOF-SIMS results of PEA (**a**) and An (**b**) treated perovskite films. An^+ signals are detected near the top film surface. Both PbI_2^+ and FA^+ display a drop in intensities when the sputtering time exceeds 900 s, as the sputtering process reaches the bottom region of the perovskite layer and thus there are fewer perovskite materials available for removal. **c.** Comparison of ligand distribution between PEA and An treated perovskite films. FA^+ signals are plotted for the PEA (dotted points) and An (solid points) samples as the reference. All plots are derived from raw data without normalization.

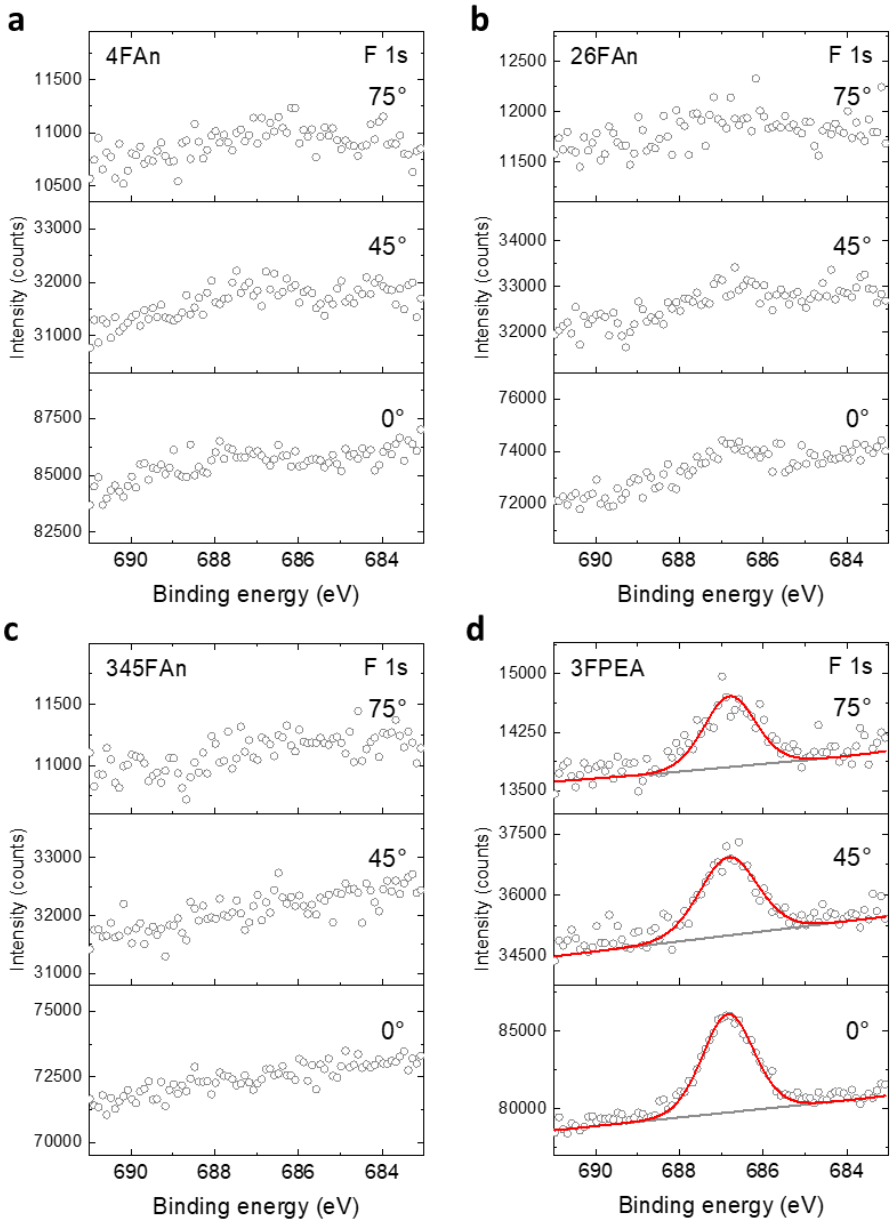

Fig. S4. XPS F 1s region of perovskite films at the electron take-off angle of 0°, 45°, and 75°: **a-c,** 4FAn (**a**), 26FAn (**b**), and 345FAn (**c**)-treated films show negligible C-F signals. **d,** The C-F peak is observed for 3FPEA-treated perovskites at different electron take-off angles. The red peak fits the C-F bond.

5

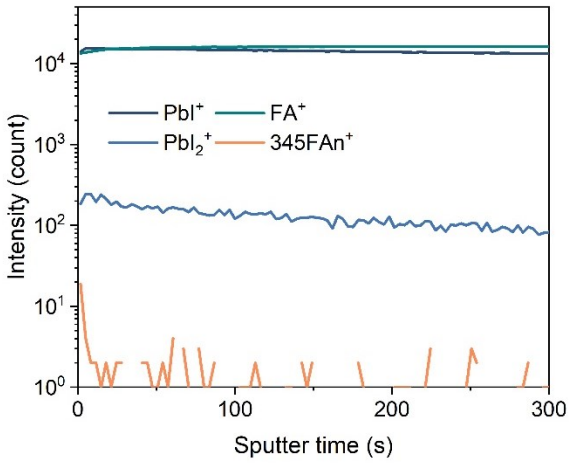

Fig. S5. TOF-SIMS results of 345FAn-treated perovskite films.

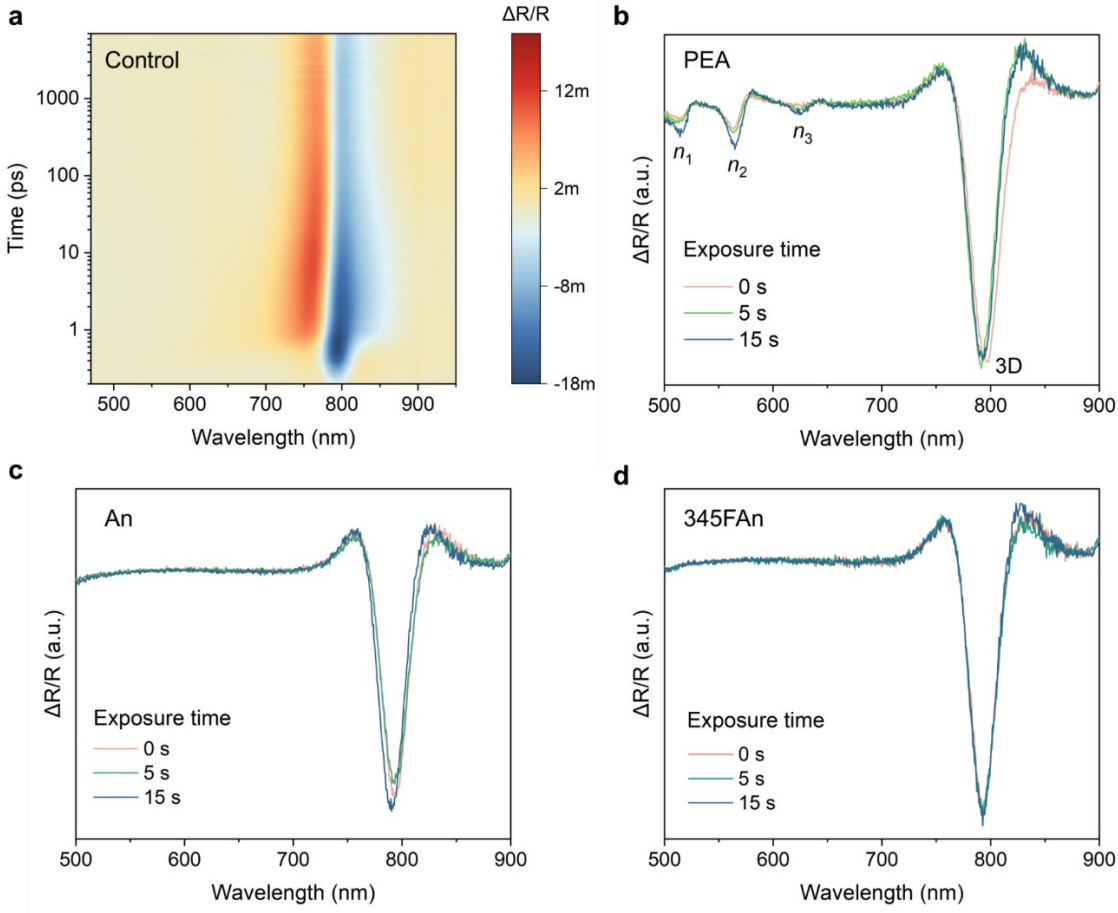

Fig. S6. a, Pseudocolour plot of ΔR/R as a function of incident photon wavelength and delay time for the control perovskite film. **b-c,** TR spectra of the PEA (**b**), An (**c**), and 345FAn (**d**) treated perovskite films at the pump-probe delay time of 410 fs, as a function of the solution exposure time. n = 1, 2, and 3 2D perovskites were found for the PEA-treated films, and their relative proportion to 3D perovskites is increased when the exposure time is prolonged. For An and 345FAn treated films, no 2D phases were detected, irrespective of the exposure time. It is noted that TR spectroscopy is utilized only for examining the phase distribution of quasi-2D perovskites, while photoinactive δ-$FAPbI_3$ and PbI_2 are detected by GIWAXS.

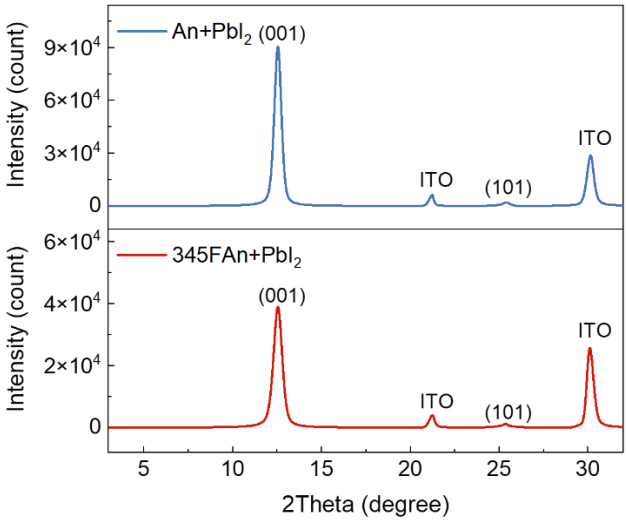

Fig. S7. XRD patterns of mixed An+PbI_2 (top) and 345FAn+PbI_2 (bottom) films. The (001) and (101) diffraction peaks of PbI_2 are observed. There are no 2D-related diffraction peaks for either film.

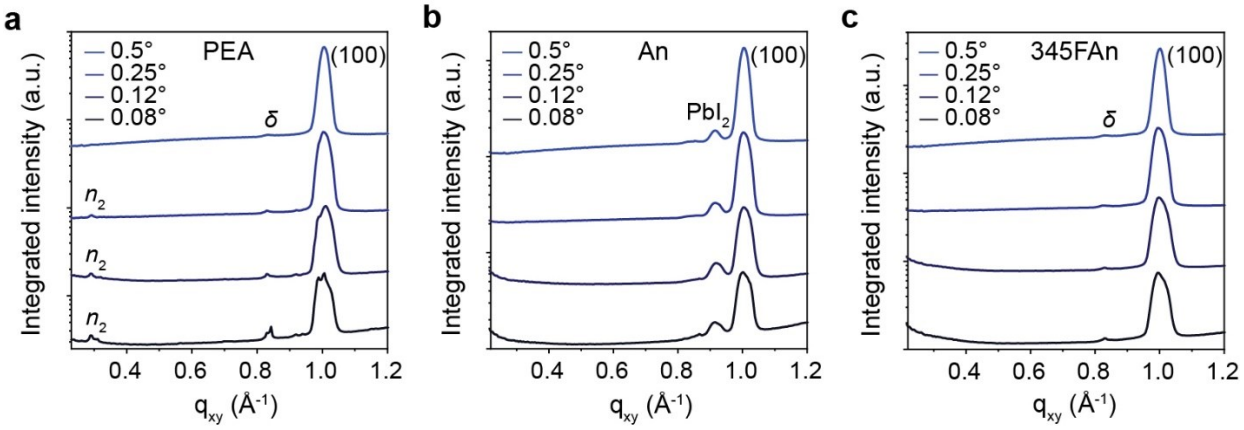

Fig. S8. GIWAXS spectra as a function of incidence angle 0.08°, 0.12°, 0.25°, and 0.5°: **a-b,** Cuts near the q_z axis of GIWAXS measurements for PEA (**a**), An (**b**), and 345FAn (**c**) treated perovskite films. $n = 2$ 2D perovskites (n_2) were observed in the PEA-treated films only at low incidence angles, indicative of the preferable presence of 2D perovskites on the film surface. PbI_2 was observed in the An-treated films due to surface degradation. δ indicates the hexagonal perovskite phase.

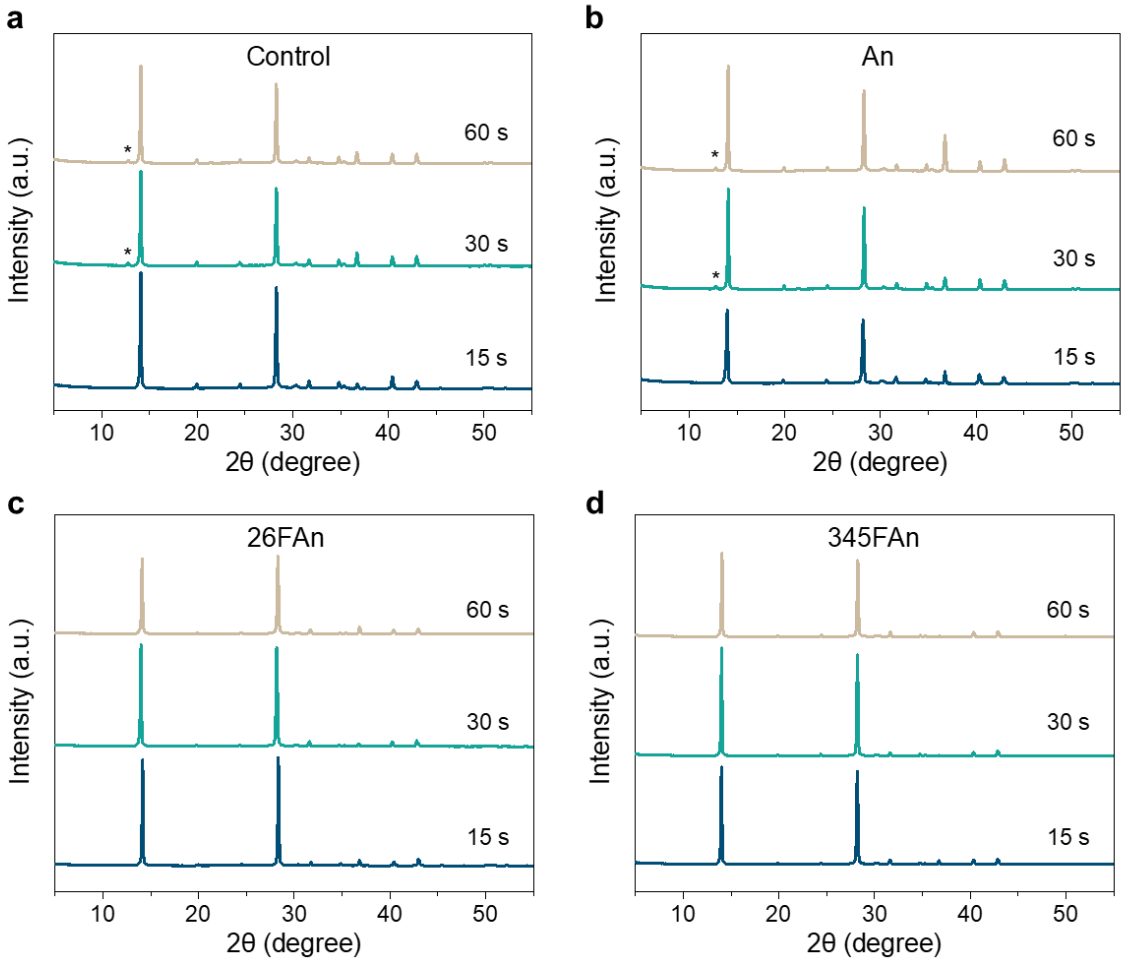

Fig. S9. XRD patterns of perovskite films with varying solution exposure times: **a,** XRD patterns of control perovskite films. The asterisk symbol (*) indicates PbI_2 species. **b-d,** XRD patterns of 4FAn (**b**), 26FAn (**c**), and 345FAn (**d**) treated perovskite films. The generation of PbI_2 during exposure to both pure solvent and An-solution is comparable, which suggests that the decomposition of perovskites is caused by solvents. Films exposed to 26FAn and 345FAn solution exhibited minimal PbI_2 generation, indicating these ammonium ligands can protect perovskites from degradation more efficiently than An.

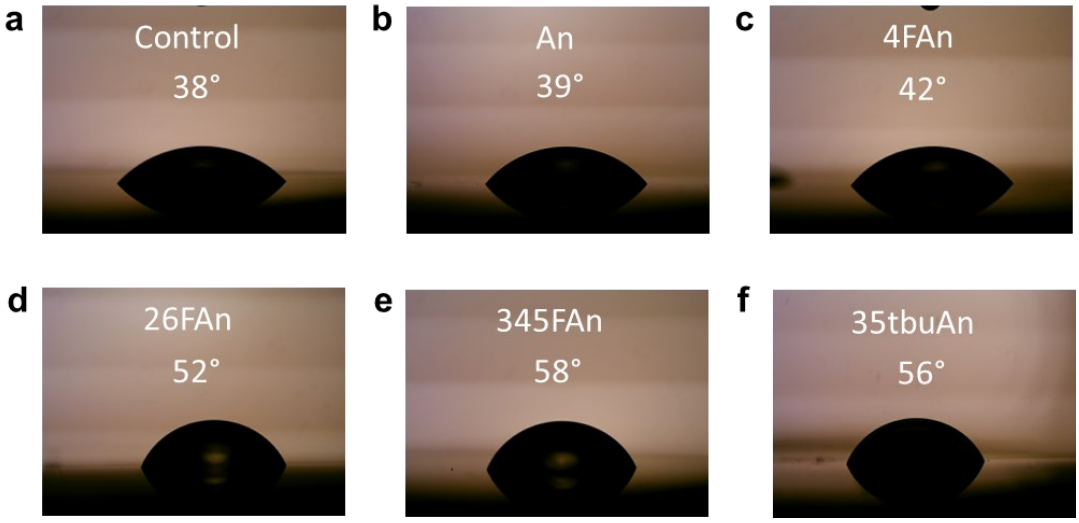

Fig. S10. Contact angle images of control and various ammonium ligand-treated perovskite films: **a-f,** The images of the water droplet for control (**a**) and An (**b**), 4FAn (**c**), 26FAn (**d**), 345FAn (**e**), and 35tbuAn (**f**) treated perovskite films. All images are recorded 2 s after the DI water drop was placed on the surface.

5

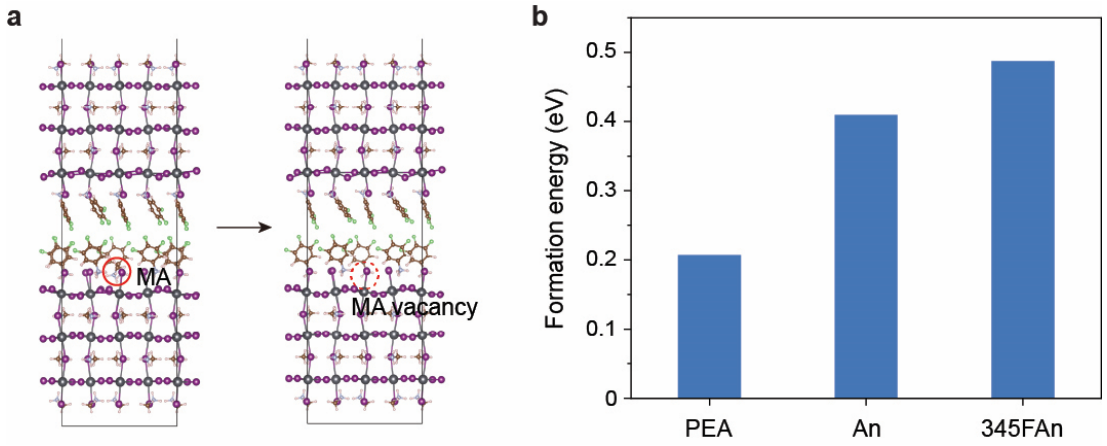

Fig. S11. DFT analysis of MA vacancy formation in various intercalated 2D/3D interfaces: **a,** Computational models used to determine the MA vacancy formation energy in the case of 345FAn intercalation. **b,** MA vacancy formation energies for PEA, An and 345FAn intercalation. Compared to PEA, the removal of MA cations becomes energetically less favorable for An and 345FAn.

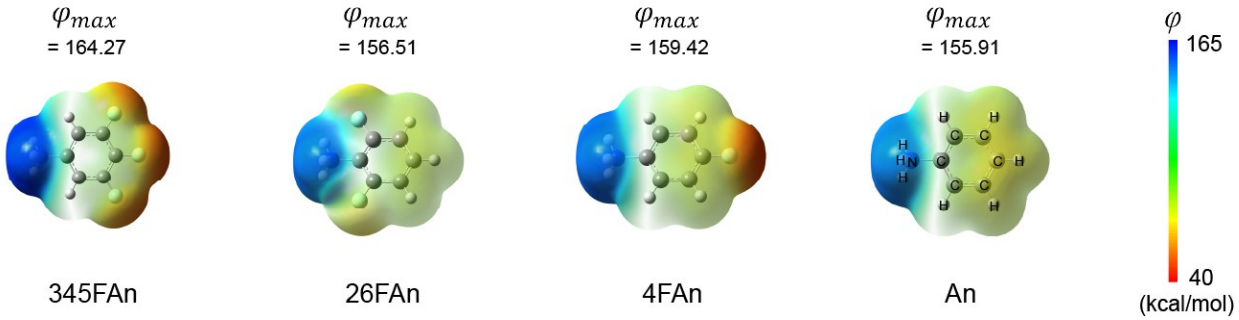

Fig. S12. Gaussian calculated electrostatic potentials (φ) of An and fluorinated An ligands. The right color bar from red to blue marks the increase of electro positivity. The φ_{max} is the maximum electrostatic potential amplitude of a specific ligand (*57*).

5

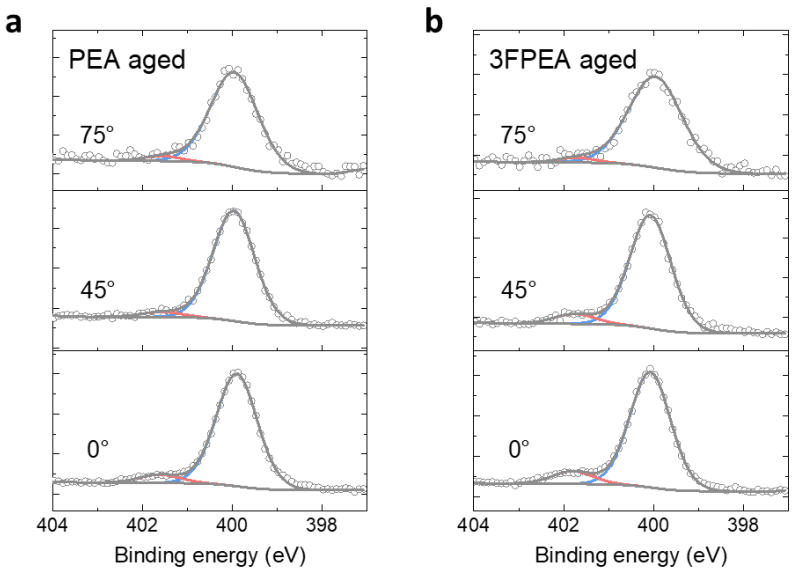

Fig. S13. AR-XPS N 1s region of aged perovskite films as a function of the electron take-off angles 0°, 45°, and 75°: **a,b,** PEA (**a**), and 3FPEA (**b**) treated films measured after 85°C annealing for 2 h. The pink peak fits the C-N bond and the blue to the C=N bond. At a 75° electron take-off angle, the C-N signals diminish significantly in comparison to the fresh sample for both films, suggesting decreased surface presence due to ligand penetration.

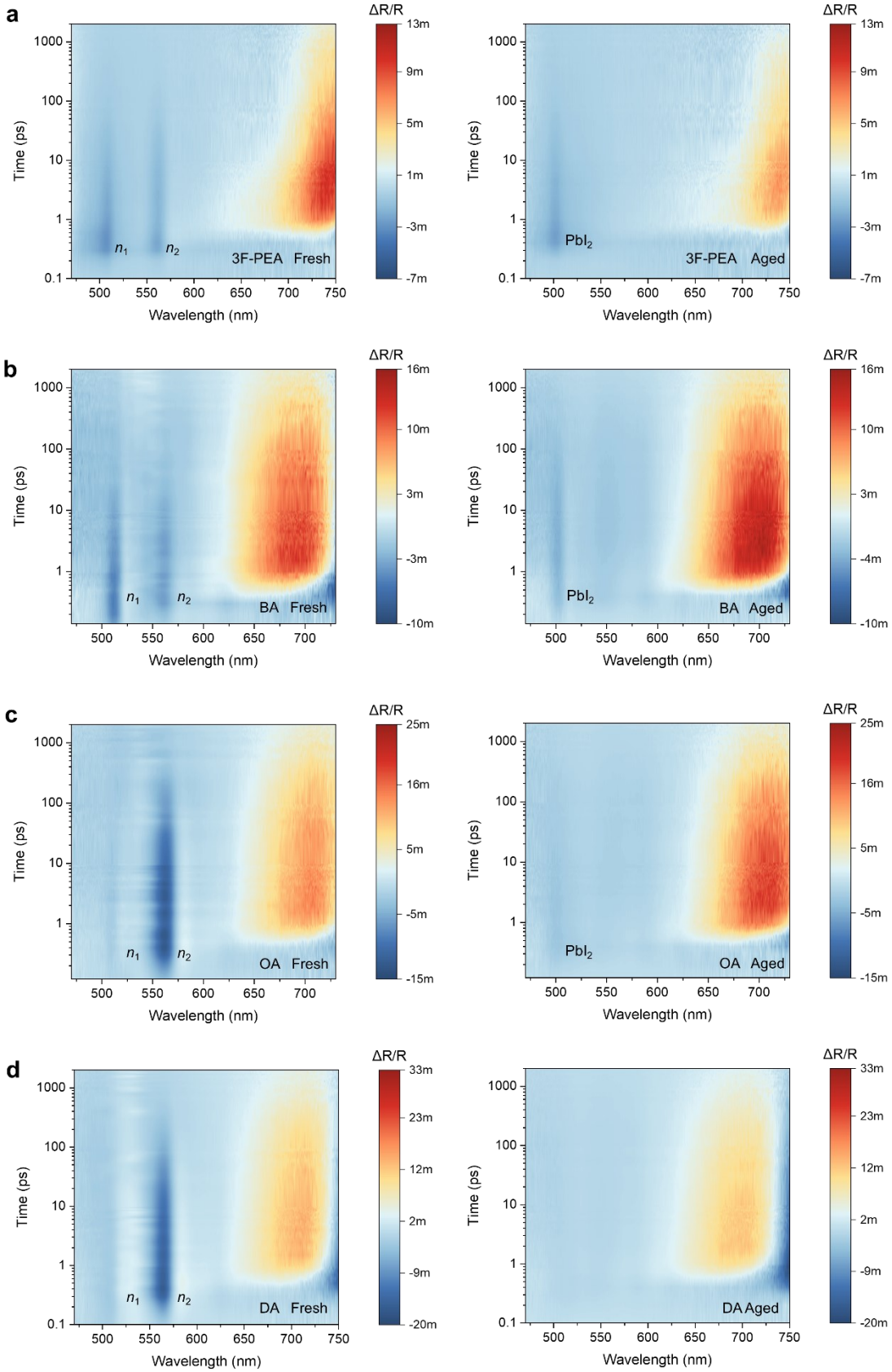
a
Time (ps)
Wavelength (nm)
ΔR/R
13m
9m
5m
1m
-3m
-7m
n_1
n_2
3F-PEA Fresh
PbI_2
3F-PEA Aged
b
16m
10m
3m
-3m
-10m
BA Fresh
BA Aged
-4m
c
25m
16m
5m
-5m
-15m
OA Fresh
OA Aged
d
33m
23m
12m
2m
-9m
-20m
DA Fresh
DA Aged

Fig. S14. Phase stability of penetrating ammonium ligand-treated perovskite films: **a-d,** Pseudocolor representation of the transient reflectance spectra for 3FPEA (**a**), BA (**b**), OA (**c**), and DA (**d**) treated perovskite films before (fresh) and after (aged) thermal aging at 85°C for 2 h. All 2D phases disappeared from the film surfaces after thermal aging.

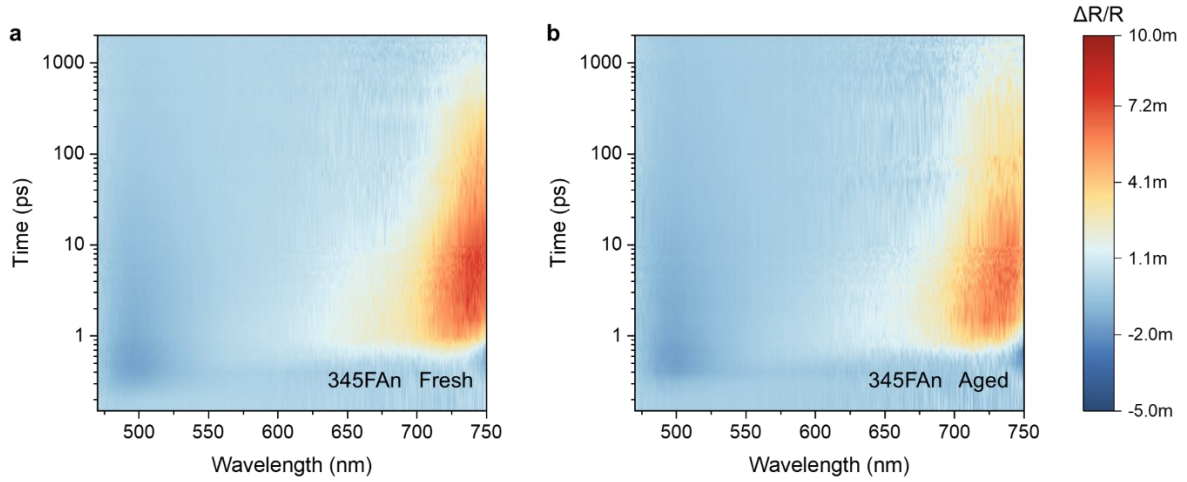

Fig. S15. Phase stability of 345FAn treated films at elevated temperatures: **a,b,** Pseudocolor representation of the transient reflectance spectra for the 345FAn treated perovskite film before (**a**) and after (**b**) thermal aging at 85°C for 2 h. No apparent phase change was observed after thermal aging.

5

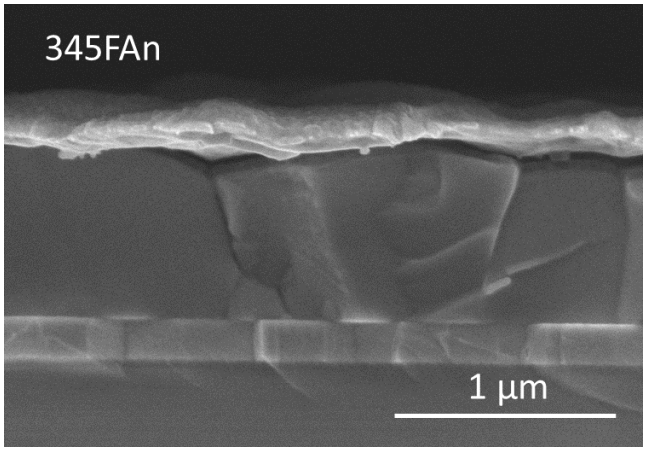

Fig. S16. Cross-sectional SEM image of 345FAn treated inverted PSCs. Scale bar = 1 µm.

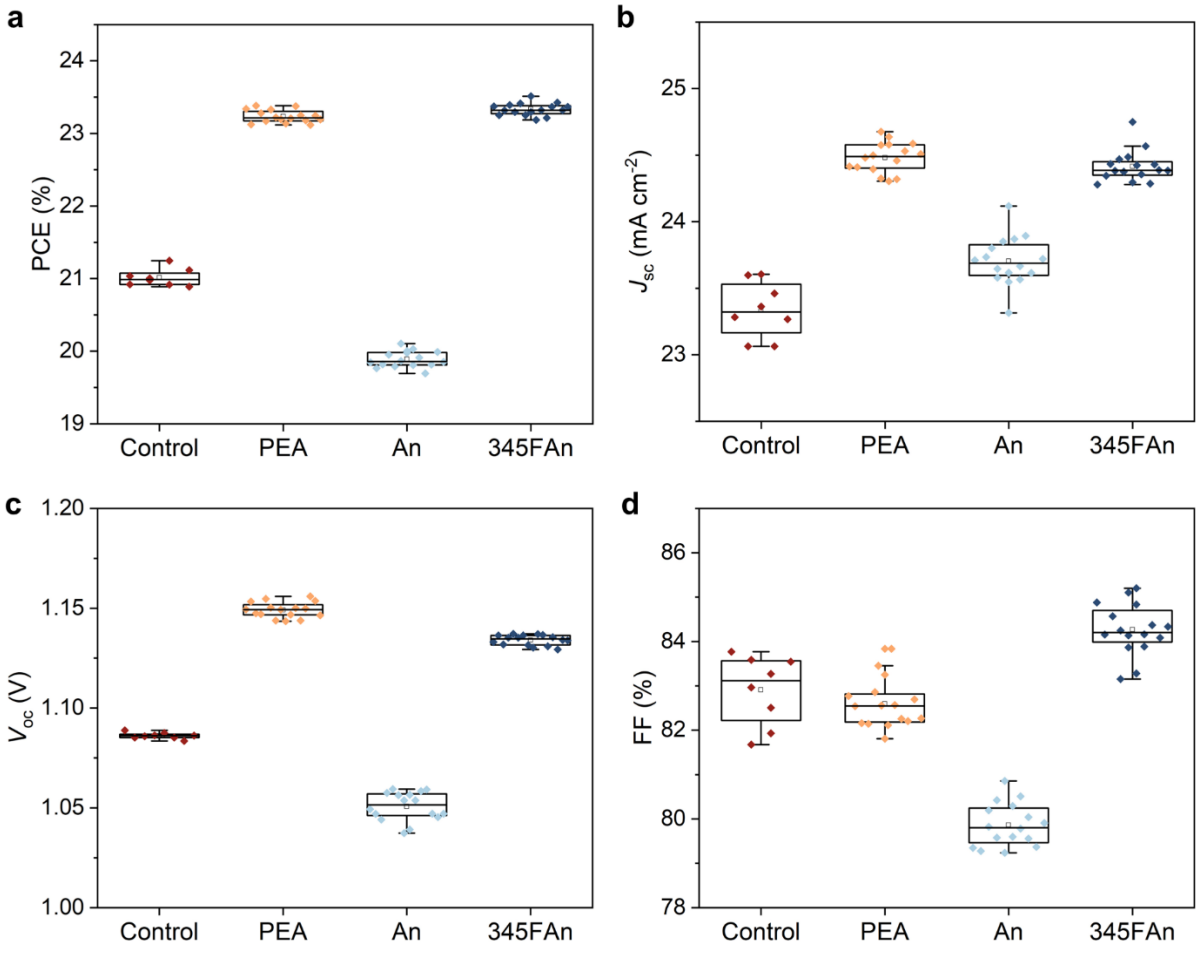

Fig. S17. Performance of control and treated PSCs: **a-d,** PV parameters, including PCE (**a**), J_{sc} (**b**), V_{oc} (**c**), and FF (**d**), of control devices (8 devices) and treated PSCs (16 devices for each type).

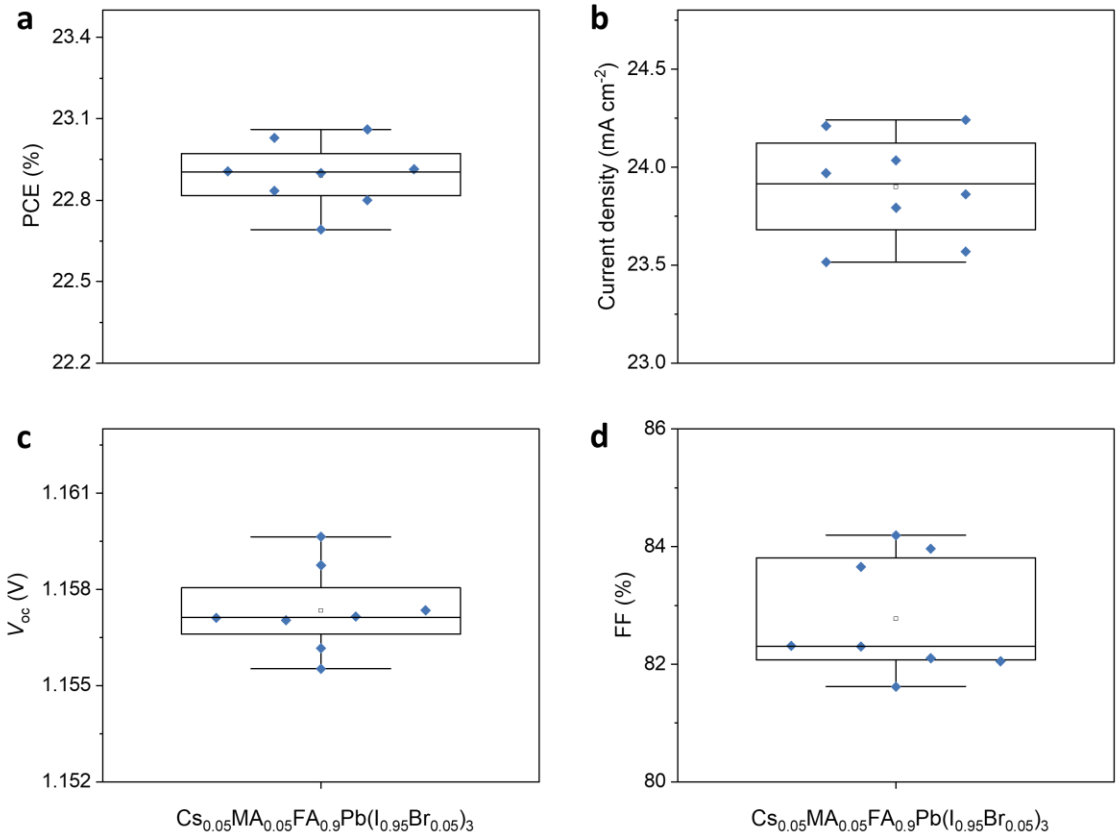

Fig. S18. PV parameters of treated $Cs_{0.05}MA_{0.05}FA_{0.9}Pb(I_{0.95}Br_{0.05})_3$ devices: **a-d,** PCE (**a**), J_{sc} (**b**), V_{oc} (**c**), and FF (**d**) of 345FAn-treated devices (8 devices). Statistical distribution is represented in box-and-whisker plots (line within the box: median, box limit: 25th and 75th percentiles, whiskers: outliers).

5

University of Toronto
1-J Perovskite Cell

Device ID: SMP 1-4
4:47 PM 11/8/2022
Spectrum: ASTM G173 global

Device temperature: 25.0 ± 0.2 °C
Device area: 0.05031 cm^2 ± 0.5%
Irradiance: 1000.0 W/m^2

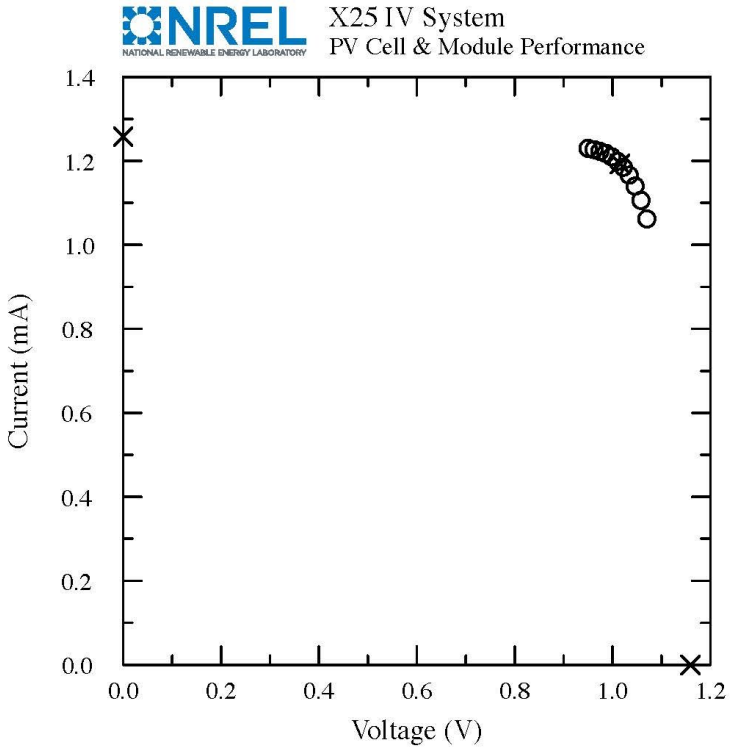

V_{oc} = 1.1595 ± 0.0018 V
I_{sc} = 1.259 ± 0.010 mA
J_{sc} = 25.02 ± 0.31 mA/cm^2
Fill Factor = (83.05 ± 0.82) %

I_{max} = 1.1935 ± 0.0098 mA
V_{max} = 1.0154 ± 0.0023 V
P_{max} = 1.212 ± 0.010 mW
Efficiency = (24.09 ± 0.30) %

Asymptotic IV
Elapsed time: 705 s.

Fig. S19. Certified results of the inverted PSC with 345FAn passivation.

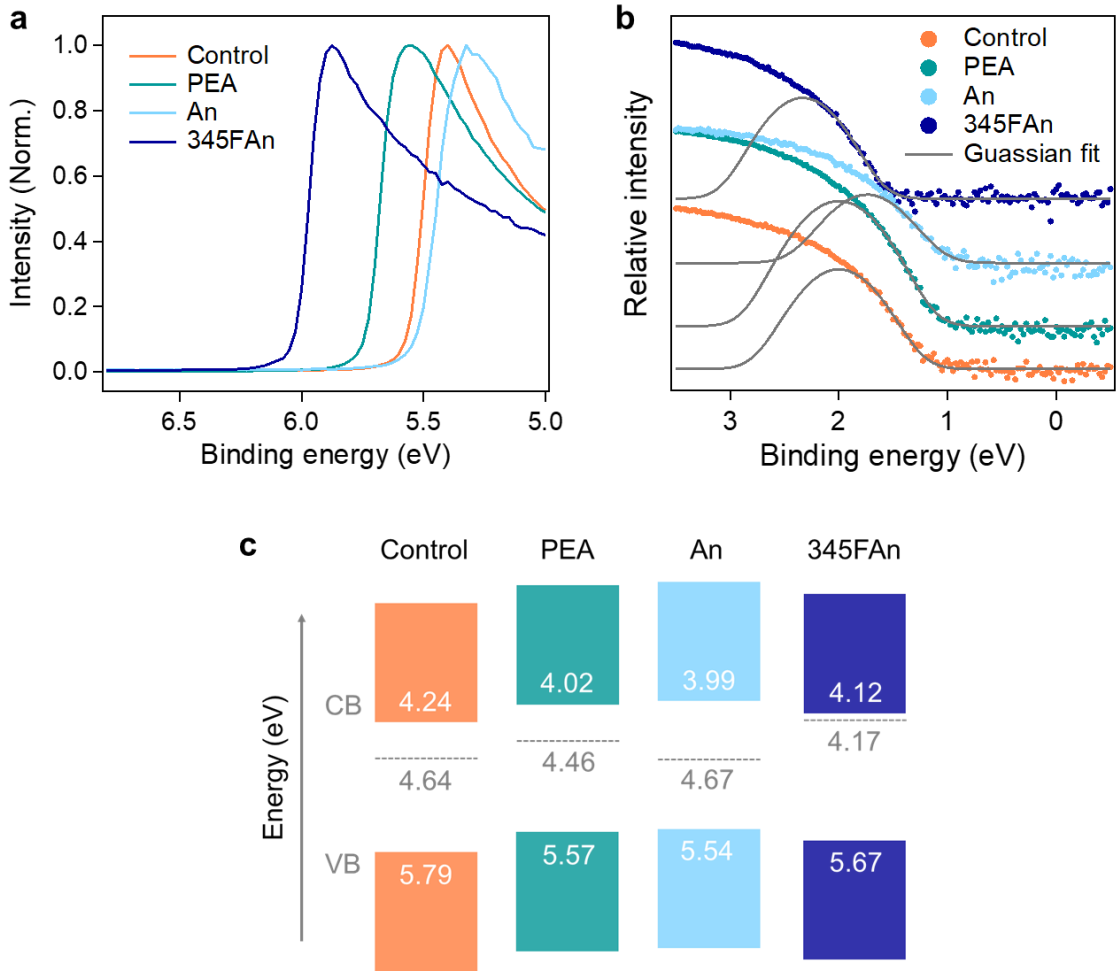

Fig. S20. UPS spectra and energy level schematic: **a,b,** Secondary electron cut-off region (**a**), and valence band onset region (**b**) plotted on a relative logarithmic scale of control and ammonium ligand treated films. The x-axis energy scale is with respect to the Fermi energy. Gaussian fit (grey solid line) was used to determine the valence band (*58*). **c,** Energy diagram comparing the alignment between the control and ammonium ligand treated films. The dashed lines indicate work functions. 345FAn induces the n-type perovskite film.

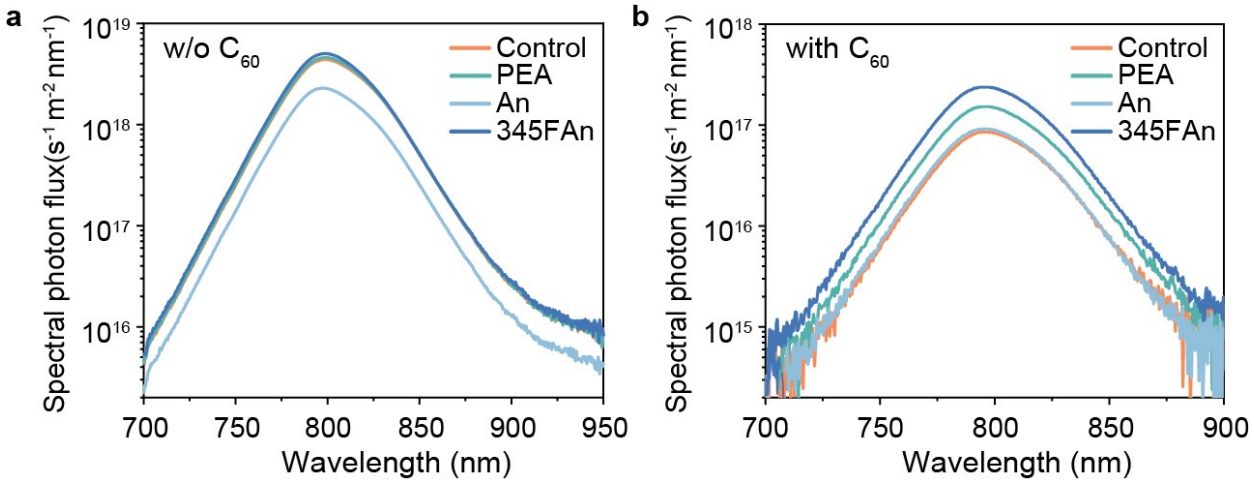

Fig. S21. a-b, Absolute intensity PL spectra of perovskite thin films on glass/ITO/2PACz without (**a**) or with (**b**) a 30 nm-thick C_{60} overlayer. The corresponding PLQY and QFLS values are summarized in Table S3.

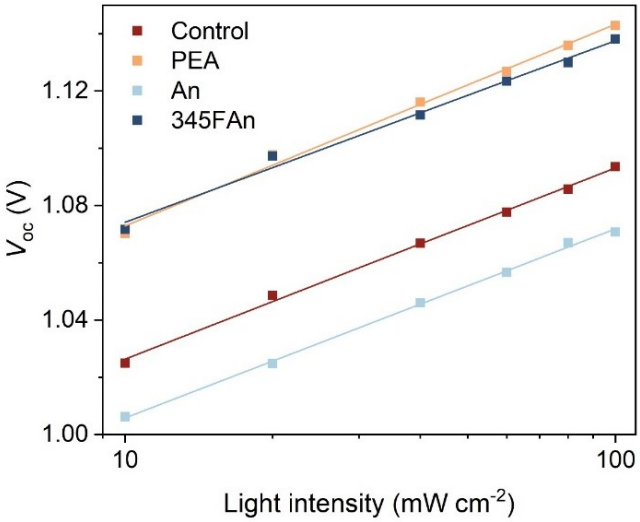

Fig. S22. V_{oc}-light intensity dependence of PSCs. The values of the ideality factor for control, PEA, An, and 345FAn devices are 1.13, 1.19, 1.12, and 1.07, respectively. It is noted that no direct correlation between ideality factor and device performance is found herein. This can be explained by recent findings: Although non-radiative bulk recombination leads to a higher ideality factor, surface and interface recombination can lead to a lower one (*59*, *60*). In addition, the ideality factor in perovskites solar cells can also be critically affected by the ionic nature of the absorber layer (*61*).

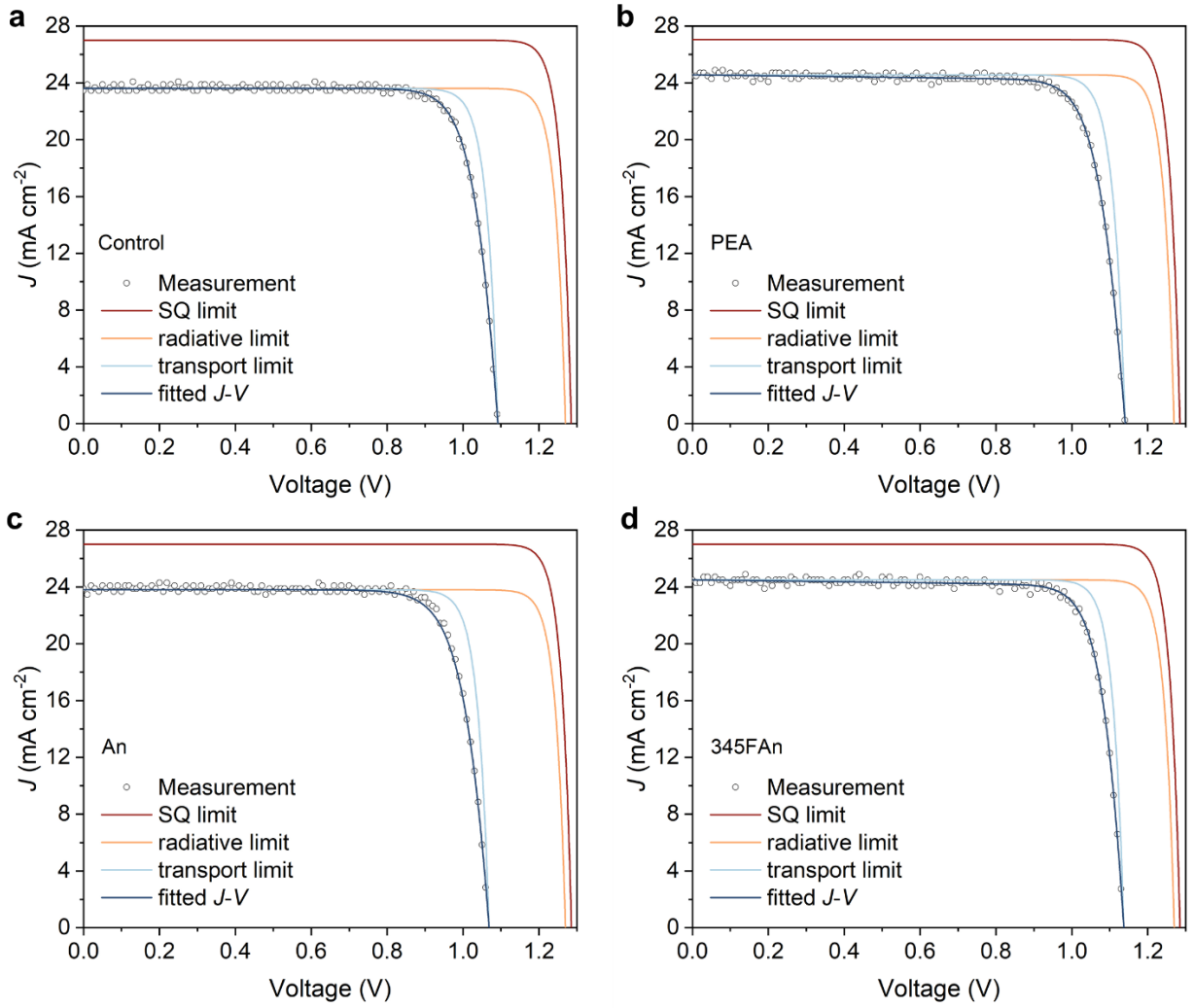

Fig. S23. a-d, *J-V* characteristics of control (**a**) and PEA (**b**), An (**c**), and 345FAn (**d**) treated PSCs. The details behind the shown *J-V* curves can be found in supplementary text. Losses due to non-radiative recombination appear in V_{oc} and FF, transport losses apparent between the transport limit *J-V* curve and the measured *J-V* curve additionally lower the FF.

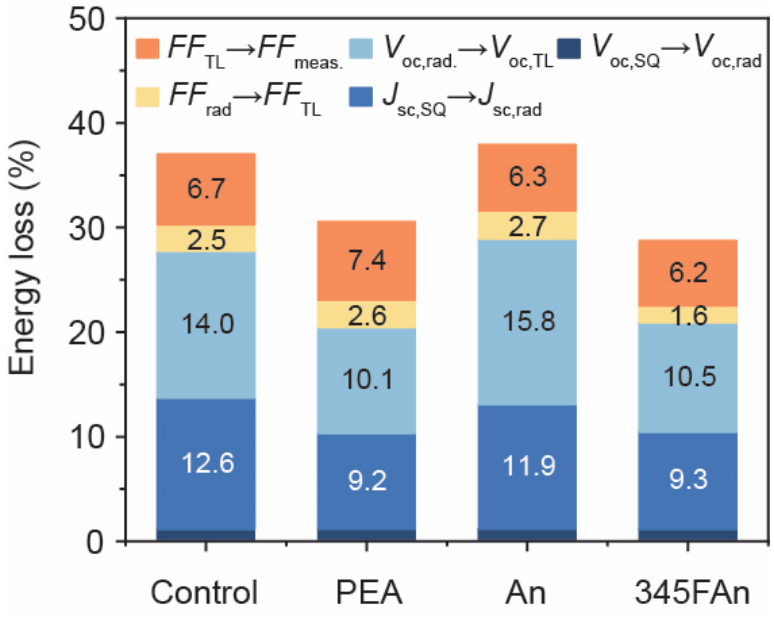

Fig. S24. Breakdown of energy loss in PSCs derived from the *J-V* fits.

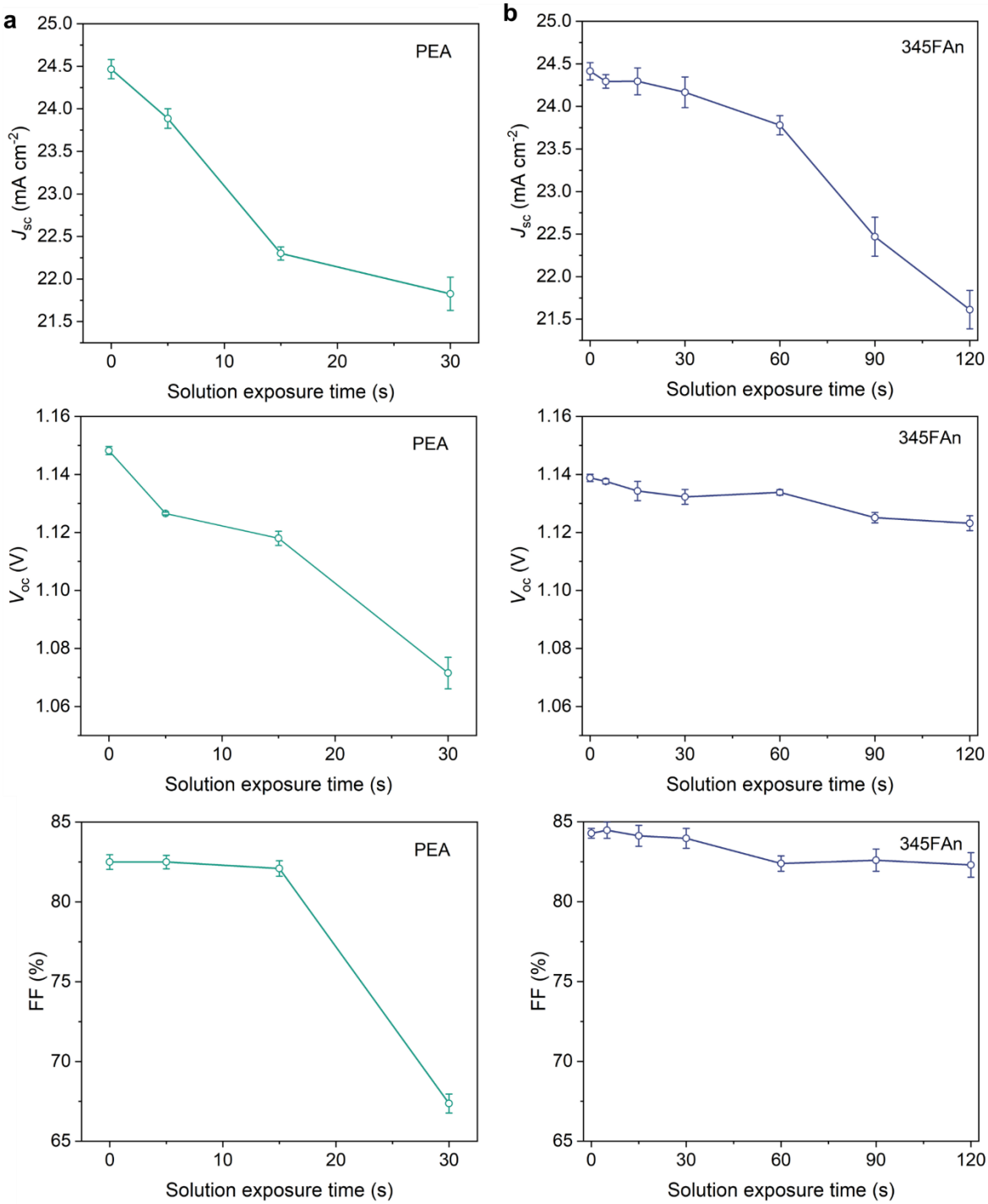

Fig. S25. PV performance of PEA and 345FAn treated PSCs as a function of solution exposure times: **a,b,** PV parameters, including J_{sc} , V_{oc}, and FF, of PEA (**a**) and 345FAn (**b**) treated devices with different solution exposure times (8 devices for each condition). Data are presented as mean values ± standard deviation.

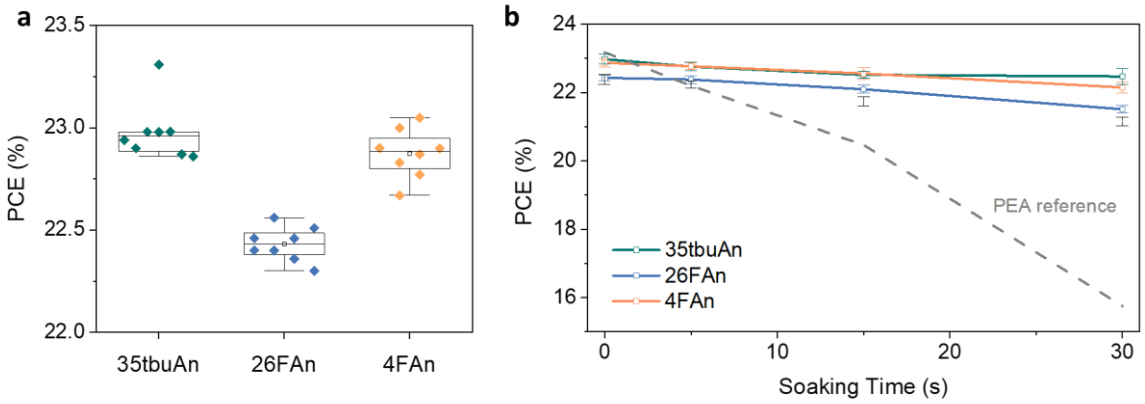

Fig. S26. Device performance of PSCs with different An-derivative passivation: **a,** PCE statistics for 35tbuAn, 26FAn, and 4FAn-treated PSCs (8 devices for each type). **b,** PCE evolution of ligand-treated devices as a function of solution exposure time (8 devices for each condition). Data are presented as mean values ± standard deviation. The grey dash line is the PCE evolution of PEA-treated devices.

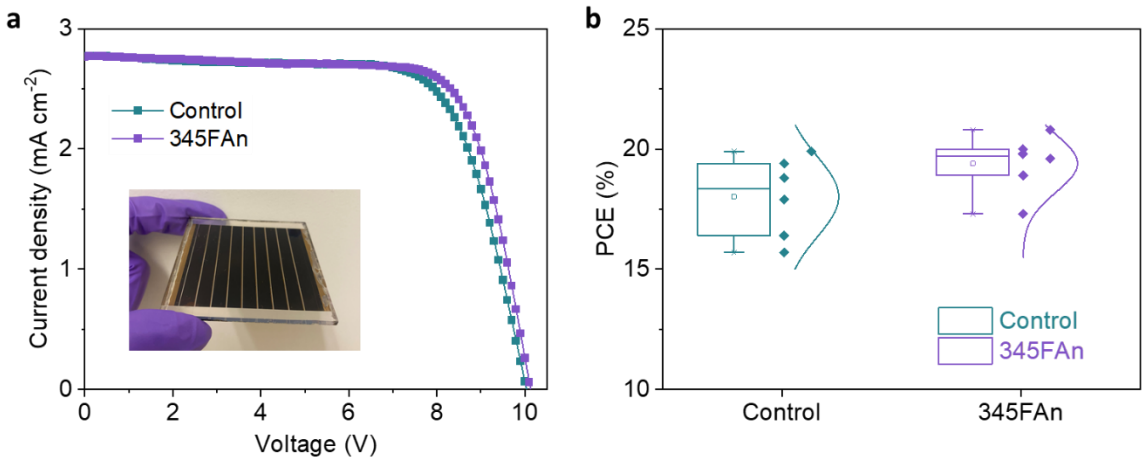

Fig. S27. Photovoltaic performance of control and 345FAn treated perovskite solar modules: **a,b,** *J-V* curves (**a**) and PCE statistics (**b**) of control and 345FAn treated perovskite solar module with an active area of 22 cm^2. Inset: Photograph of a representative perovskite solar module.

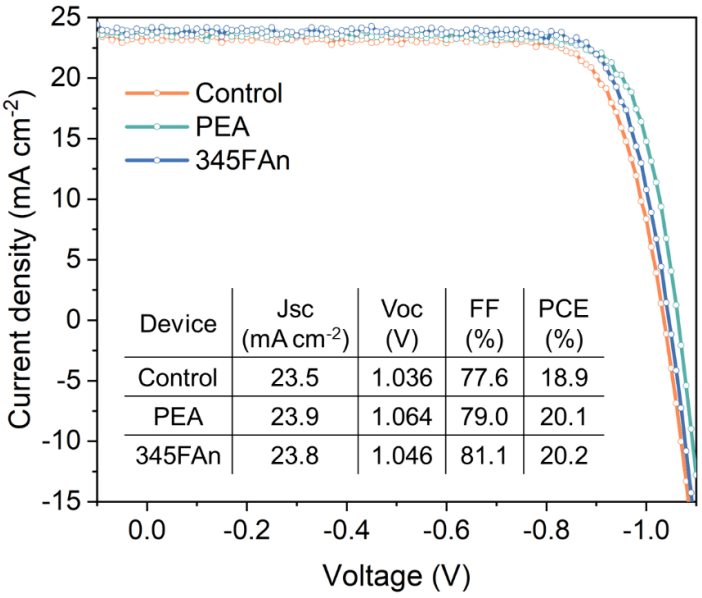

Device	Jsc (mA cm^{-2})	Voc (V)	FF (%)	PCE (%)
Control	23.5	1.036	77.6	18.9
PEA	23.9	1.064	79.0	20.1
345FAn	23.8	1.046	81.1	20.2

Fig. S28. *J-V* curves and figures of merit for devices used in stability testing. The device architecture is ITO/2PACz/Perovskite/C_{60}/ALD-SnO_x/Ag and the perovskite composition is $Cs_{0.05}MA_{0.05}FA_{0.9}Pb(I_{0.95}Br_{0.05})_3$.

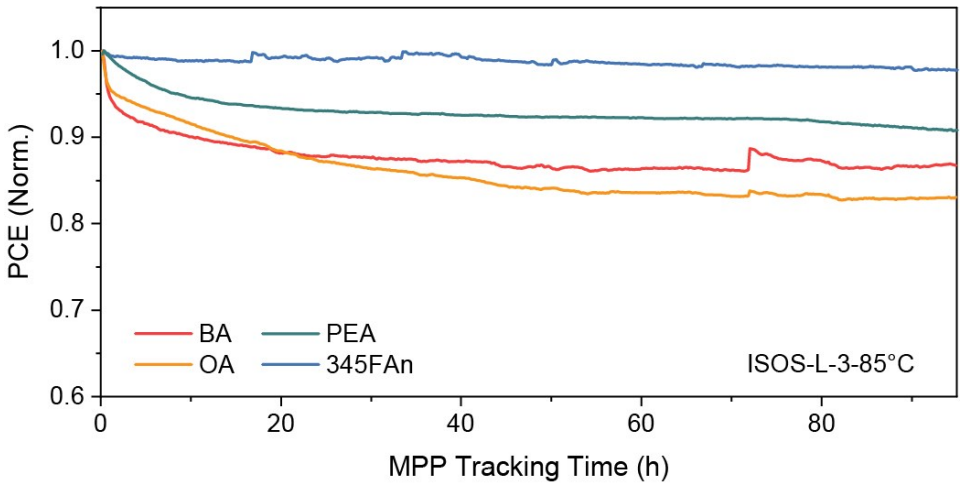

Fig. S29. MPP tracking of encapsulated BA and OA devices at 85°C with a relative humidity of ~50% under 0.8-sun illumination. PEA and 345FAn results, as presented in Fig. 5E, are included for reference.

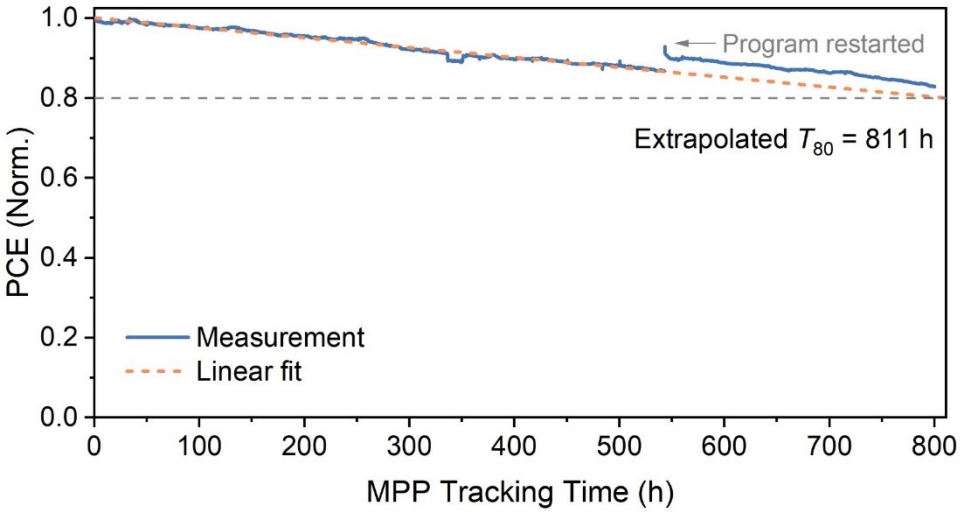

Fig. S30. Linear extrapolation of stability testing. Based on the initial 500 h stability data, we estimate the T_{80} lifetime to be ~810 h for the 345FAn-treated PSC using linear extrapolation.

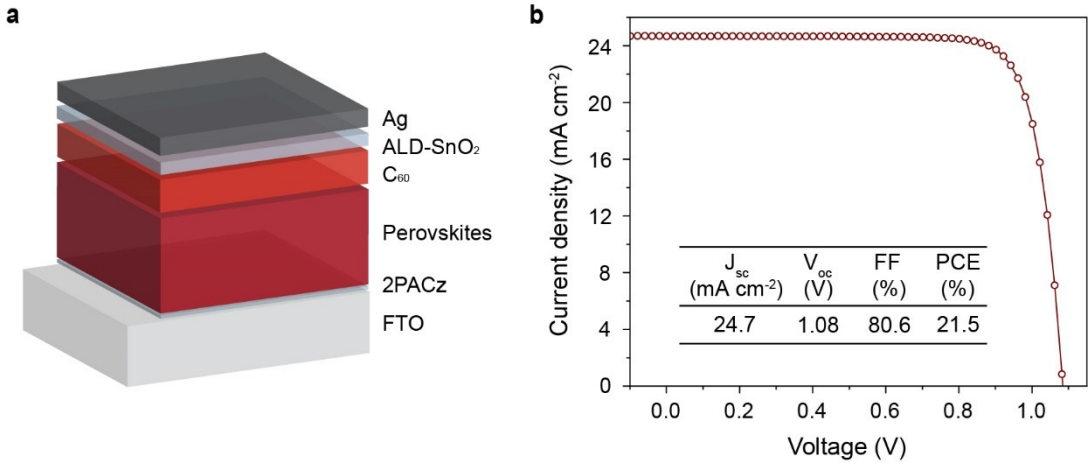

Fig. S31. a,b, The device architecture (**a**), *J-V* curve, and figures of merit (**b**) for the FTO device used in stability testing. The perovskite composition is $Cs_{0.05}MA_{0.05}FA_{0.9}Pb(I_{0.95}Br_{0.05})_3$. The *J-V* curve was measured under 1-sun-equivalent white LED illumination at room temperature.

5

Table S1. XPS peak position and area for control and ammonium-ligand-treated perovskite films at α = 0°, 45°, and 75° electron take-off angles

Films	Take-off angle (°)	C-N peak position (eV)	C-N peak area	FA N peak position (eV)	FA N peak area	C-N to FA N ratio
Control	0	401.3	0.80	400.0	18.0	0.04
	45	401.3	0.74	400.0	16.5	0.04
	75	401.4	0.91	400.1	14.2	0.06
PEA	0	401.4	1.82	399.7	14.0	0.13
	45	401.5	1.31	399.8	13.1	0.10
	75	401.6	1.25	399.8	11.4	0.11
3FPEA	0	401.6	2.14	399.9	14.2	0.15
	45	401.7	1.72	400.0	13.3	0.13
	75	401.7	1.54	400.0	10.9	0.14
BA	0	401.3	1.56	399.6	12.7	0.12
	45	401.4	1.78	399.5	10.5	0.17
	75	401.5	1.80	399.6	9.06	0.20
OA	0	401.3	2.31	399.6	14.2	0.16
	45	401.4	2.67	399.6	12.2	0.22
	75	401.4	2.38	399.6	10.5	0.23
DA	0	401.5	2.31	399.7	14.1	0.16
	45	401.6	1.58	399.9	15.2	0.10
	75	401.6	1.02	399.9	13.6	0.08
An	0	401.4	0.86	399.7	12.5	0.06
	45	401.5	0.78	399.8	15.2	0.05
	75	401.3	0.81	399.8	13.2	0.06
4FAn	0	401.5	0.57	399.9	12.7	0.04
	45	401.6	0.54	399.9	10.9	0.05
	75	401.5	0.40	399.9	7.83	0.05
26FAn	0	401.4	0.66	399.9	15.6	0.04
	45	401.4	0.64	399.9	12.8	0.05
	75	401.5	0.76	399.9	10.1	0.07
345FAn	0	401.6	0.83	400.0	16.1	0.05
	45	401.5	0.57	400.0	14.1	0.04
	75	401.7	0.77	400.0	11.7	0.06
35tbuAn	0	401.4	0.90	399.9	14.7	0.06
	45	401.4	0.68	399.9	12.4	0.05
	75	401.4	0.16	399.9	3.2	0.05

5

Table S2. Summary of quasi-steady-state (QSS) certified PV parameters of > 21% PCE inverted PSCs

V_{oc} (V)	J_{sc} (mA cm^{-2})	FF (%)	PCE	Ref.
1.1595	**25.02**	**83.05**	**24.09% (NREL)**	**This work**
1.1607	25.44	81.48	24.05% (NREL)	Q. Jiang, Nature (2022) (*45*)
1.1505	24.90	83.46	23.91% (NREL)	H. Chen, Nat. Photonics (2022) (*23*)
1.1687	22.89	84.55	22.62% (NREL)	S. Chen, Sci. Adv (2021) (*62*)
1.1429	23.84	82.0	22.34% (Newport)	X. Zheng, Nat. Energy (2020) (*63*)

Table S3. Summary of PL peak position, PLQY, $V_{oc,rad}$, and QFLS for the perovskite thin films with or without the C_{60} overlayer

Films	Overlayer	PL peak position (nm)	PLQY (%)	$V_{oc,rad}$ (V)	QFLS (eV)
Control	None	799	13.4	1.265	1.213
	C_{60}	796	0.26	1.269	1.117
PEA	None	798	13.9	1.265	1.214
	C_{60}	797	0.47	1.270	1.132
An	None	797	7.0	1.266	1.198
	C_{60}	796	0.28	1.270	1.119
345FAn	None	799	15.0	1.266	1.217
	C_{60}	795	0.73	1.271	1.144

Table S4. Summary of reported device operational stability based on ISOS-L-3 protocols.

Light source	T	Environment	Surface passivation	PCE @high-T	Lifetime	Ref.
White LED	**85°C**	**~50% RH**	**345FAn**	**19.9% (85°C)**	**T_{85} = 1560 h**	**This work**
White LED	65°C	~50% RH	3FPEA 2D/3D	N.A.	T_{92} = 500 h	H. Chen, Nat. Photonics (2022) (*23*)
Metal-halide lamp	85°C	~65% RH	$Cs_2PbI_2Cl_2$	~16.5% (85°C)	T_{85} = 4000 h	X. Zhao, Science (2022) (*12*)
Xenon lamp	85°C	~50% RH	None	~14.2% (85°C)	T_{95} = 1200 h (Post 15% burn-in)	Y-H. Lin, Science (2020) (*11*)
Plasma lamp	65°C	~60% RH	$PbSO_4$	~19.5% (65°C)	$T_{96.8}$ = 1200 h	S. Yang, Science (2019) (*18*)